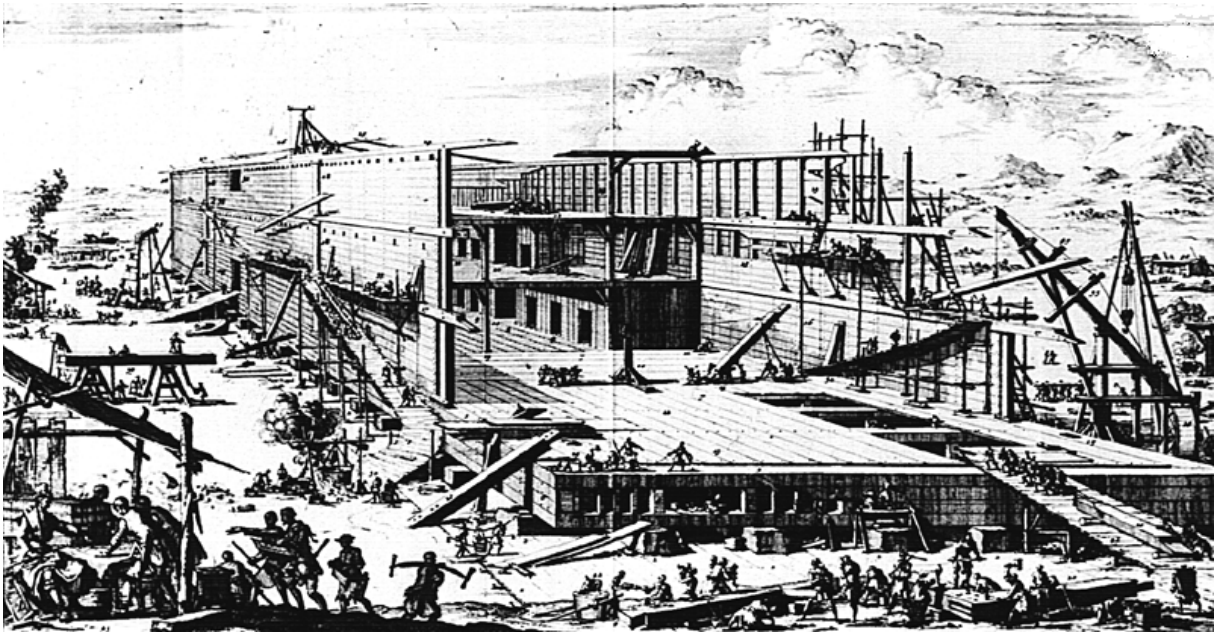# ICANOE[1]

Answers to Questions and Remarks Concerning the ICANOE Project

The ICANOE Collaboration

In Genesi 6:16 leggiamo:
"Farai nell'arca un tetto e a un cubito piu' sopra la terminerai;
(...)la farai con un piano inferiore, un secondo piano e un terzo piano".

---

[1]Imaging and CAlorimetric Neutrino Oscillation Experiment

ii

The ICANOE Collaboration

F. Cavanna, D. Mazza, G. Nurzia, S. Petrera, G. Piano Mortari, C. Rossi
Dipartimento di Fisica e INFN, Università dell'Aquila, via Vetoio, L'Aquila, Italy

M.Brigida, C.Favuzzi, P.Fusco, F.Gargano, N.Giglietto, F.Giordano, F.Loparco,
M.N.Mazziotta, A.Rainò, P.Spinelli, A.Vaccina
Dip. di Fisica dell'Università di Bari and INFN Sez. di Bari, via Amendola 173- Italy

R. Fiore, E.Lamanna, A. Papa, G.Russo
Università della Calabria and INFN

P. Cennini, A. Ferrari[1]
CERN, CH 1211 Geneva 23, Switzerland

A. Borio di Tigliole, A. Cesana, M. Terrani
Politecnico di Milano (CESNEF), INFN, via Ponzio 34/3, Milano, Italy

A. Badertscher, A. Bueno, M. Campanelli, C. Carpanese, J. Rico, A. Rubbia, N. Sinanis,
Institute for Particle Physics, ETH Hönggerberg, Zürich, Switzerland

C. Chen, Y. Chen, K. He, X. Huang, Z. Li, F. Lu, J. Ma, G. Xu, C. Zhang, Q. Zhang,
S. Zhen
IHEP – Academia Sinica, 19 Yuqnan Road, Beijing, People's Republic of China

S.V.Golovkine, A.M.Gorine
Institute for High Energy Physics, Moscow, Russia

R.A.Mukhamedshin, G.T.Zatsepin
Institute of Nuclear Research, Moscow, Russia

V.A.Smotryaev, I.S.Trostin
Institute of Theoretical and Experimental Physics, Moscow, Russia

K.V.Alexandrov, V.A.Chechin, A.P. Chubenko, A.D.Erlykin, F.F.Kayumov,
S.K.Kotel'nikov, E.P.Kuznetsov, B.N.Lomonosov, G.I.Merzon, V.A.Ryabov,
V.O.Tikhomirov, V.A.Tsarev
P.N.Lebedev Physical Institute, Moscow, Russia

P.Bernardini, I.De Mitri, G.Mancarella
Dip. di Fisica dell' Università di Lecce and INFN Sez. di Lecce, via Per Arnesano - Italy

F. Arneodo, E. Bernardini, A.Di Credico, A.Grillo, O. Palamara, E.Scapparone
Laboratori Nazionali di Gran Sasso, INFN, S.S. 17bis, km 18+910, Assergi (AQ), Italy

---

[1]Also at Dipartimento di Fisica e INFN, Università di Milano, via Celoria 16, Milano, Italy

D. Cline, C. Matthey, S. Otwinowski, H. Wang, J. Woo

Department of Physics, UCLA, Los Angeles, CA 90024, USA

A.M.Baranov, E.T.Gushchin, V.A.Kantserov, A.A.Semak, S.V.Somov

Moscow Engineering Physical Institute, Moscow, Russia

G. Battistoni, D. Cavalli, P. Sala, T. Rancati

Dipartimento di Fisica e INFN, Università di Milano, via Celoria 16, Milano, Italy

M.Ambrosio, C.Aramo, G.C.Barbarino, D.Campana, F.Guarino, A.Lauro, A.Ordine,
G.Osteria, V.Palladino

Dip.di Scienze Fisiche dell' Università di Napoli and INFN Sez.di Napoli, via Cintia -Italy

B. Babussinov, S. Centro, G. Meng, D. Pascoli, F. Pietropaolo, S. Ventura

Dipartimento di Fisica e INFN, Università di Padova, via Marzolo 8, Padova, Italy

P. Benetti, R. Brunetti, E. Calligarich, R. Dolfini, A. Gigli Berzolari, F. Mauri,
L. Mazzone, C. Montanari, A. Piazzoli, A. Rappoldi, G.L. Raselli, M. Rossella,
C. Rubbia, D. Scannicchio, P. Torre, C. Vignoli, Z. Xu

Dipartimento di Fisica e INFN, Università di Pavia, via Bassi 6, Pavia, Italy

F. Sergiampietri

INFN Pisa, via Livornese 1291, San Piero a Grado (PI), Italy

P. Picchi[2]

University of Torino, Torino, Italy

G.V.Gavalian, R.L.Kavalov, M.P.Lorikian

Yerevan Physical Institute, Yerevan, Armenia

---

[2]Also at Laboratori Nazionali di Frascati, INFN, Frascati, Italy and Istituto di Cosmogeofisica, CNR,
Torino, Italy

This is an open Collaboration and other Participants are being invited to join Institutes that have already expressed their interest

P. Assimakopoulos, I. Papadopoulos, P. Pavlopoulos, V. Vlachoudis
University of Ioannina, Greece

V.A. Matveev, E.N. Goloubeva, A.V. Kovzelev, O.V. Kazachenko, A.V. Polarush, V.E. Postoev, I.N. Semeniouk, A.N. Toropin
Institute of Nuclear Research, Moscow, Russia

P. Razis, A. Vorvolakos
University of Cyprus, Cyprus

Contents

Chapter 1

Summary of questions

A summary, including our basic answers to the questions (in italic in the text) proposed by the referees after the presentation of the ICANOE proposal to the September Meetings of the SPSC and LNGSSC, is followed by a few sections containing a more detailed discussion of the various subjects.

1.0.1 September Meeting of the SPSC

1. Physics:

   - *The NOE part of the project requires more physics simulations in order to illustrate its role in improving the physics output.*

     The improvements in number of signal events and in the control of its separation from background, making use of the improved reconstruction of minimum bias events, is detailed in chapter 2.

   - *ICANOE seems to be suitable to obtain information on the full mixing matrix - more information than given in 5.6 on the $\nu_\mu \to \nu_e$ oscillation search would be welcome (in particular, a more detailed discussion on the influence of the beam systematics).*

     A discussion of this point as well as of the beam systematics can be found in chapters 4 and 3 respectively.

   - *is the Δm^2 determination as discussed in Section 5.5.4 really justified in view of the possibility of ν_μ oscillating into ν_s or a small possible addition of the ν_μ oscillating into ν_e?*

     The $\nu_\mu \to \nu_e$ case is discussed in details in chapter 4. The problematics associated with the oscillation into ν_s will be better addressed in the future.

   - *ICANOE vs. KamLAND - what is the overlap in the ICANOE physics capabilities with respect to KamLAND, taking into account that ICANOE will start to take data a few years later? How about T600 which will start to take data at the same time as KamLAND?*

2. Apparatus:

- *What are the reasons for the delay of the T600 module with respect to the schedule presented to the SPSC in 1997?*

  We have been funded for the cryogenics and purification systems for the T600 only in the second half of 1997. The supply contract foresees the delivery and complete installation of the dewar and of the related cooling and purification systems within three years from the contract signature.

  According to the supply contract with Air Liquide Italia, the full engineering design has been carried on between the second half of 1997 and the first half of 1998. The basic engineering design (dated 1996) was largely modified, also due to the results of a first test on a 10 m^3 prototype, co-funded by INFN and Air Liquide and run between 1996 and 1997.

  To verify the new design Air Liquide considered necessary the construction (at no charge) of a second 10 m^3 prototype, which was successfully tested during the first half of 1998. This test postponed the beginning of the first half-module assembly of about 8 months. This is the delivery delay that we actually suffer from.

  As far as the internal detector mechanics is concerned, the full engineering design was completed in the second half of 1998. The commissioning of the last components (for the HV system for the drift) was made in June 1999. We expect the delivery of all the mechanical parts to be completed by February 2000. We have also some delay for the internal detector mechanics, mainly due to the slowliness of the bureocratic procedures for the bids.

  However, we would like to notice that, besides the above mentioned delays, starting from 1997 we have built a fully equipped experimental hall with a clean room larger than 1000 m^3 inside. The new 10 m^3 prototype was installed and tested into this hall.

  The assembly island for the internal detector was also realized and the site is now prepared to host the cryostat (the insulation basement and supports are installed).

- *Which is the minimal number of supermodules to get a significant physics result for tau appearance? In principle Figure 5.15 gives an answer but may be it is worth to make a strong point for the four-supermodules configuration.*

  Four supermodules are required, with the planned 4 year duration of the CNGS beam, to explore fully the Δm^2 region allowed by SuperKamiokande with adequate statistical significance.

- *Are the proposed four NOE modules really necessary? Could one or two modules be sufficient? It would be worth to justify the proposed configuration with four modules by physics simulations.*

  The discussion of the physics requirements for the ICANOE calorimetric modules can be found in chapter 2.

- *A discussion of possible staging scenarios would be useful.*

  The ICANOE detector is inherently modular. Therefore it lends itself naturally to a number of possible, graded strategies. For more details we refer to our

Proposal [1]. The main input element – still missing in order to provide a specific scenario – is the actual availability of space in the Gran Sasso Laboratory, a decision which has to be taken by the Management. In particular, one has to know if the full Hall B is to be dedicated for ICANOE or if, for instance, two experiments will have to share the space. In this latter case, the detailed interaction between them will have to be carefully studied, in order to understand if and how a succession of different installations could be carried out.

1.0.2 September Meeting of the LNGSSC

- *The question of the optimisation of the relative mass and distribution of the liquid and solid calorimeters was also raised at the meeting. Could the arguments or criteria leading to the optimisation be explained,if as it was claimed the optimisation depends on the overall length,two scenarii could be used for this length.*

  The criteria and physics requirements leading to the optimisation of the solid and liquid targets can be found in chapter 2.

- *It is planned in Icanoe to drift inside the modules over 4 m of liquid Argon ,this is close in Hv to the tested limit of the feedthru, what safety margin do you judge necessary between test and regular operation? Is it possible to test the 3m drift on one of the T600 half modules?*

  The relevant parameters here are the maximum drift time and the electron lifetime. The maximum drift time is linearly dependent on the electron lifetime, while at the typical field we plan to use, the dependence on the field is weaker. Provided the electron lifetime is long enough (> 5 ms) we can safely operate the detector at voltages well below the limits of the present feedthrough design. We plan to start the operation at 250 V/cm corresponding to a maximum drift time of 4 ms and a maximum operating voltage of 100 kV.

  The internal detector of one of the 600 T half-modules could be reconfigured for the 3 m drift operations. In principle this test could also be performed in the 10 m^3 prototype equipped with a chamber with a vertical drift.

- *The Icanoe proposal uses a calorimetric (i.e. non-imaging) readout of the liquid Argon at the ends of modules. Again is it possible to test this concept in the second T600 half module?*

  A solution is already under test in the 10 m^3 prototype, as it is described in chapter 5.

- *What is the trigger scheme to be used in the running of Icanoe? For events contained in the liquid calorimeter, could you test the trigger with the T600 modules?*

  The ICANOE detector will operate simultaneously on Cosmic Ray (CR) and Beam (BB) events, which will have priority over CR during the short SPS burst. The triggering for CR is based on a minimum energy loss inside the Argon, for instance at a threshold of $50 \div 100$ MeV. The installation of photo-multipliers inside the LAr and the consequent observation of the calorimetric light emitted offers a natural way

on which to construct the trigger logic. As an alternative, we can use the induced signal on the high voltage plane due to the drifting charges. Preliminary tests have shown that such a signal can also be used, with a threshold comparable to the one indicated above. The trigger is also intended to provide a determination of the $t = 0$ time, necessary to determine the absolute position of the event inside the Argon, primarily for those events which do not cross drift boundaries.

The triggering for BB events is simply a gate window which is opened during the short (30 μs) burst from the SPS. In the case of BB events the previous information from LAr and from the NOE calorimeters in an OR condition can be used to further perfect the trigger efficiency and to provide a better $t = 0$ information.

We finally remark that the trigger condition has to be injected only at the end of the very long read-out time, simply in order to avoid that the information on the event, contained in the memory of the continuously sensitive LAr is overwritten. This leaves ample time (milliseconds, depending on the size of the buffer) for an intelligent, second level trigger which is performed by the on-line processors of the read-out, to which the actual topology of the event is being supplied.

- *The size of the Icanoe cryostats are larger than the T600 modules and therefore cannot be assembled in Pavia and transported as complete unit. Could you present a scenario and solutions for assembly of the modules in the underground hall; can you have an estimate of the man years necessary on site for this operation.*

All the informations available in this moment are reported in the Preliminary Technical Design starting from chapter 2.

Chapter 2

The role of the magnetized calorimeter

The search for ν_τ appearance requires detectors with high performances, in event imaging, energy reconstruction and particle identification. The liquid argon technique has unique bubble chamber like imaging features, and a high precision energy determination.

As in the past, when bubble chambers were complemented by external electronic detectors, a combined scheme of alternating liquid/solid sections has been considered in the ICANOE proposal.

The main contributions of the solid detector to the physics outputs concern mostly the detailed analysis of minimum bias events (i.e. ν_μCC interactions) and therefore the control of energy calibrations and backgrounds. Its denser sections reduce the transverse and longitudinal size of charged current neutrino events, acting effectively as a focusing device of both the muon and the accompanying shower. The calorimetric role of the solid detector is imposed by the need of continuing to sample the shower development also in this sections. As shown in Fig.2.1 the calorimeter complements LAr hadronic energy measurements for neutrino interactions occurring in the last part of the LAr volume ($\sim$ 3 m), allowing thus to fully exploit the imaging capabilities of the the entire LAr volume.

The addition of the solid detector provides:

1. larger acceptance in angle and momentum (through measurements of range and magnetic analysis) for muons, as well as sign selection of a large fraction of them;

2. fast and reliable reconstruction and monitoring of the characteristics of the ν_μ beam, including its $\bar{\nu}_\mu$ contamination;

3. an absolute energy calibration reference, based on a robust and proven technique, for the calorimetric response of the LAr.

In addition the solid detectors also contribute to the oscillation signal sensitivity. The increase of the LAr fiducial mass (20%) and the several additional ktons (50%) of the solid target permits to detect a larger number of events originating from oscillations both of beam and atmospheric neutrinos.
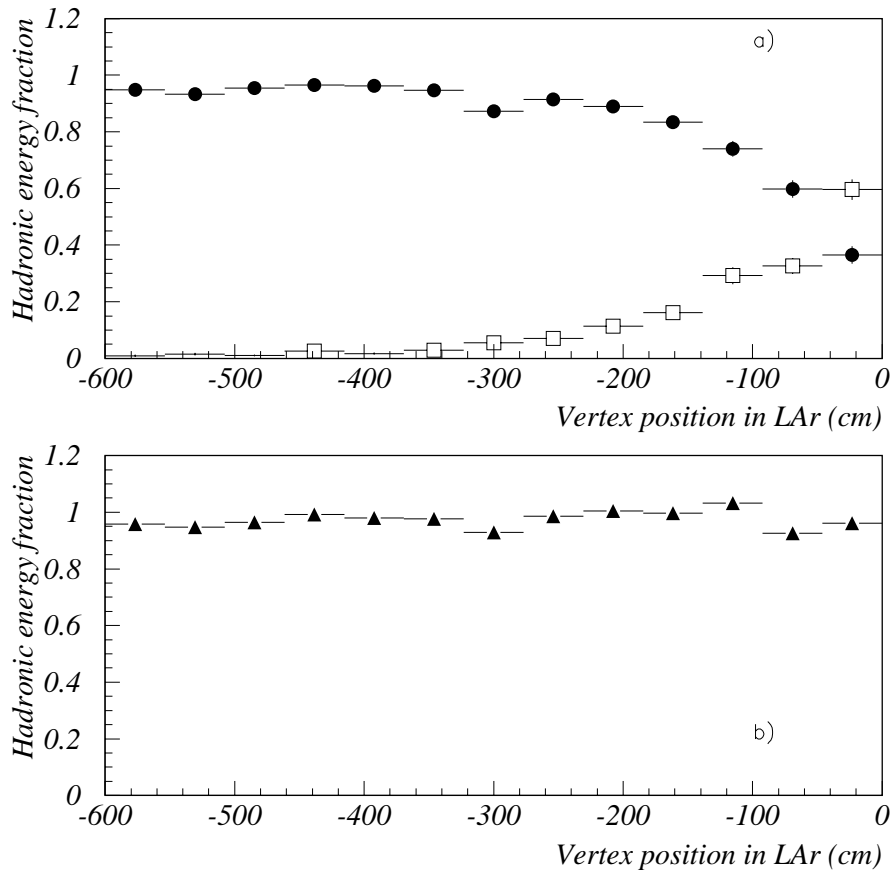
Figure 2.1: a) Percentage of hadronic energy in the two subdetectors as a function of the vertex position for neutrino ν_τCC interactions occurring in the last six meters of argon; (solid circles: LAr, squares: calorimeter) b) Total fraction of reconstructed energy

It should also be noted that the confinement of each event (apart the muon) in one supermodule makes each of them an independent detector capable of running also in case of failure of its neighbors.

Sect. 2.1 discusses the contributions of the solid detector to the understanding of charged current neutrino interactions and to the general calibration of the detector. Sect. 2.2 discusses its contribution to the search for neutrino oscillations, i.e. the improvements in the number of signal events and in the control of its separation from background due to the improved reconstruction of minimum bias events.

This discussion allows also to reach a conclusion on the optimal number of solid detectors. In this optimization procedure we have been guided by the following considerations:

1. The number of ν_τ events should by no means be reduced. The total target mass of liquid argon has been fixed at the ~ 5.6 kton value assumed in the proposal;

2. The maximum length of each liquid argon module has been assumed to be 16 m, as dictated by safety and present construction experience;

3. The overall cost of the argon subdetectors increases if shorter modules are used; no

length shorter than 8 m was considered.

It turns out in the end that the detector configuration with four pairs of liquid and solid modules presented in our proposal is a good compromise between physics output and overall cost, and that a lower number of solid modules would result in a smaller sample of signal events and a worse control of the background.

2.1   Muon momentum measurements and sign discrimination

Muon momentum can be measured by the magnetic analysis in the spectrometer (in this case muons are required to cross at least one solid module) or through range measurement for those stopping inside the detector. Muon momentum measurements through multiple scattering in LAr is well suited for atmospheric low energy events. Its use as a complement of the magnetic measurement will be investigated in the future.

A GEANT3 simulation including all detector details has been performed for three different detector configurations. In order to optimize the number of solid detectors we have simulated configurations with four liquid argon modules and with a number of calorimeters along the apparatus ranging from one to four, as shown in fig. 2.2. ν_μCC events with vertex in LAr have been generated. In order to select a sample of events useful for CNGS beam monitor and studies of minimum bias interactions, events have been required to deposit at least 90% of the hadronic energy in the sensitive volume (LAr or calorimeter).

Fig 2.3 shows the percentage of these events with the muon momentum measured in the spectrometer, as a function of the amount of LAr in front of each calorimeter module. For these events the muon sign can be also determined. As can be seen from this figure, the configuration with four LAr modules and four calorimeters modules (labelled 16 m in the figure) is much more satisfactory in term of acceptance with respect to configurations with a smaller number of calorimeters. We also note that the gain in acceptance in the hypothesis of 8 m LAr modules each followed by a calorimeter module (labelled 8 m in the figure) is rather small and is not balanced by the doubled cost of the calorimeter and by the additional costs of shorter LAr modules.

2.1.1   Neutrino beam monitor

Different event categories (fully contained in LAr, fully contained in calorimeter, and events sharing their energy in both subdetectors) can be used to reconstruct the ν_μ beam spectrum. Fig. 2.4 shows the number of ν_μCC events per year surviving the requirements quoted in the previous section and with the muon momentum reconstructed by magnetic measurement or by range, for the three different detector configurations. In this plot the contributions of interactions in the liquid and solid target are shown separately. The increase in the rates with the number of calorimeters comes from the larger acceptance, as shown in Fig.2.3 and from the contribution of the mass of the additional calorimeter modules. Muons produced by interactions occurring in the last calorimeter module, i.e.

the one closing the detector downstream the beam, do not meet the requirement for muon reconstruction and give a negligible contribution to the total rate.

The final statistics collected in the four calorimeter configuration ($\sim$ 11000 events/year) allows to reach a reasonable control of the beam in a few months of data taking.

2.1.2   Detection of antineutrino events

As shown in Fig. 2.3 the magnetic spectrometers, in the configuraton with 4 solid detectors, provide the sign of the muon for about 60% of the CC events originating in the liquid argon.

In table 5.6 in the ICANOE proposal a total rate of about 1100 $\bar{\nu}_\mu$ events is estimated in the liquid target for an exposure of 20 kton $\times$ year. This corresponds to about 2 % of the main ν_μ component. We expect to collect therefore a sample of about 650 $\bar{\nu}$ events identified as such by the presence of a positive muon. One can therefore measure the antineutrino contamination present in the beam and its average energy with a typical statistical uncertainty of 5 % or less.

This measurement is important per se; a significant discrepancy in the detected rate of antineutrino events or in the average value of their energy could signal new unexpected phenomena in the propagation of neutrinos. A result consistent with the expected 2% contamination on the contrary would give confidence in our capability of simulating correctly, besides the main component, also the contaminations present in the beam. A correct prediction of the detected $\bar{\nu}_\mu$ event rate would result in increased confidence in the prediction of the beam composition and spectra.

A possible exploitation of the CNGS in antineutrino mode has also been discussed in [2] and in [1] and is indeed likely to take place at a later stage. The 10 times larger contaminations that are predicted in this beam should and will be comfortably measured by means of the ICANOE magnetic spectrometers.

2.1.3   Hadronic energy calibration of the liquid argon

Liquid argon hadronic calorimetry requires an absolute energy calibration reference, based on a reliable and precise technique. Scintillating fiber calorimeter has been extensively calibrated at PS-T7 (see Chap. 11 in [1]) and further tests are foreseen in the near future. LAr calibration can be achieved by comparing the reconstructed neutrino beam spectra from events fully contained in the liquid and events fully contained in the solid target. Such a procedure requires an adequate statistics of the data samples originating in both subdetectors. The number of events in the calorimeter useful for inter-calibration is shown in Fig. 2.5 for the different detector configurations.

As an example of the inter-calibration procedure, we consider the reconstruction of the ν_μCC spectrum using ν events originating in LAr and those originating in one calorimeter. The shape of the uncorrected spectrum reconstructed by the LAr (dotted line) and by a single calorimeter (solid points) is shown in Fig. 2.6 (top). Looking at the figure, the two reconstructed spectra seem to be compatible within the statistical error. The expected 20% shift arising from the LAr visible energy before calibration is masked by the poor

statistics. Fig. 2.6 (bottom) shows the same spectra obtained using four calorimeters. The higher statistics makes possible to appreciate the shift in ν_μCC shape reconstructed with the two subdetectors. The complementarity between the liquid and the solid targets allows an intercalibration and a precise LAr visible energy experimental determination on site independently of montecarlo calculations.

The final statistics for the detector configurations with one calorimeter is therefore too poor and is not sufficient to achieve a reliable LAr calibration.

2.1.4   Calibration of muon energy measurements

In ICANOE the measurement of the muon energy can be performed with different methods:

- *range* - for muons stopping in the apparatus

- *MS* - analysis of multiple scattering effect on sufficiently long tracks in LAr [3]

- *magnetic method* - analysis of track bending in the magnetized calorimeter

When the muon track is sufficiently long in both subdetectors, the last two methods can be applied together. Such redundancy allows the intercalibration of the two techniques and a better muon momentum reconstruction.

In Fig. 2.7 we show the muon track lengths in both the subdetectors for "transition" events. The plot has been divided in four regions assuming 2.5 m as a minimum length needed for the magnetic reconstruction and 5 m for the MS method[1]. In region A only the MS method can be applied, while in sector D the magnetic measurement alone can be used. In region B both methods are available thus allowing their intercalibration. The range method can also be used when the muons stop in the CAL, providing the reconstruction of the most of the events in region C.

We expect that ~ 45 % of the beam ν_μ CC events in LAr are in region B ($\sim 2.5 \times 10^4$ events for 20 kton $\times$ year).

---

[1]The threshold values depend both on the μ energy and required momentum resolution.
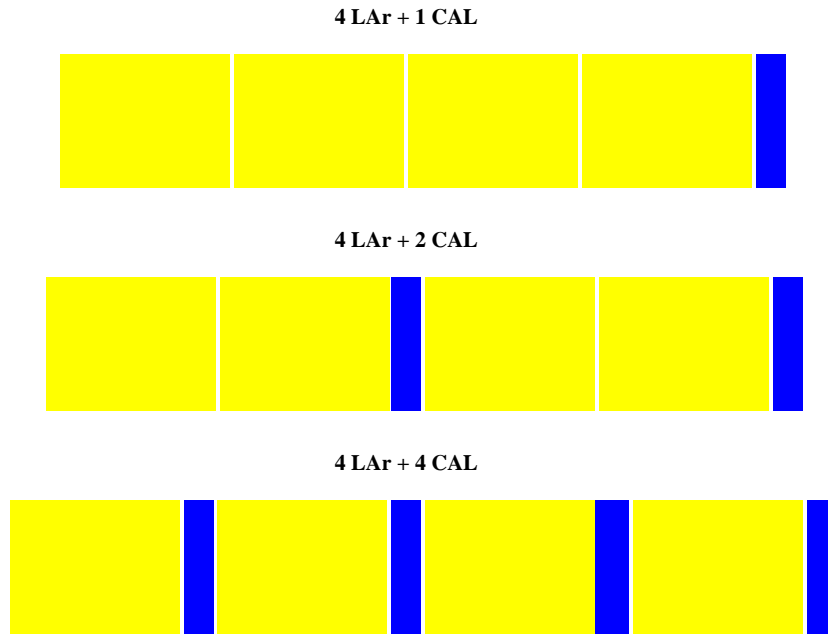
4 LAr + 1 CAL

4 LAr + 2 CAL

4 LAr + 4 CAL
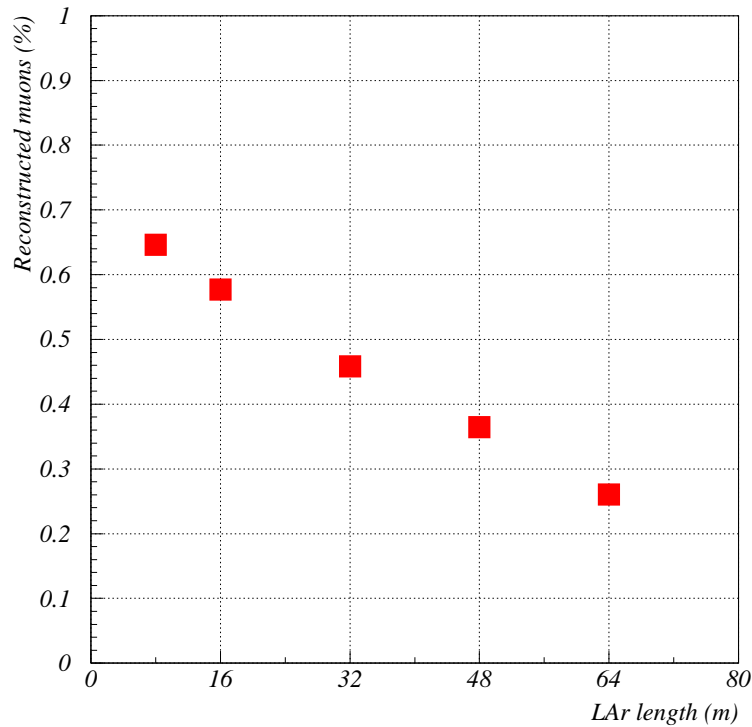
Figure 2.2: The three simulated detector configurations

Figure 2.3: Percentage of reconstructed ν_μCC events with vertex in LAr, with muons measured through magnetic measurement in the spectrometer. 16 m of LAr length corresponds to the configuration with four LAr modules and four calorimeter modules (Fig.2.2c)), 32 m to the configurations with four LAr modules and two calorimeter modules (Fig.2.2b)), 64 m to the configurations with four LAr modules and one calorimeter module (Fig.2.2a))
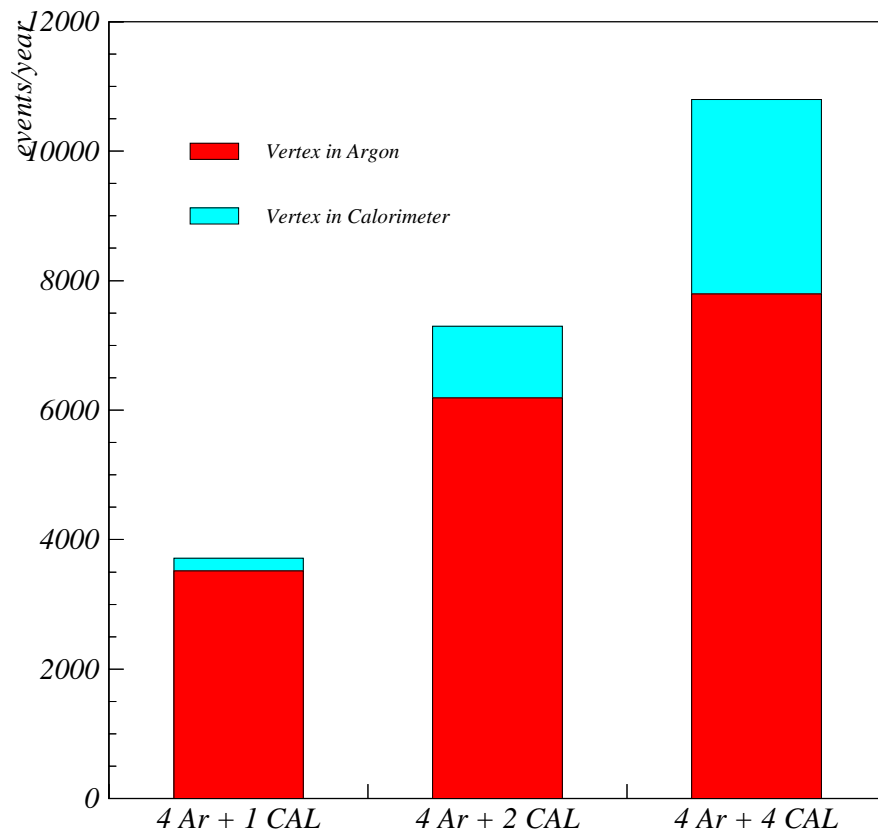
Figure 2.4: Expected total statistics of ν_μCC reconstructed events, for the three simulated detector configurations
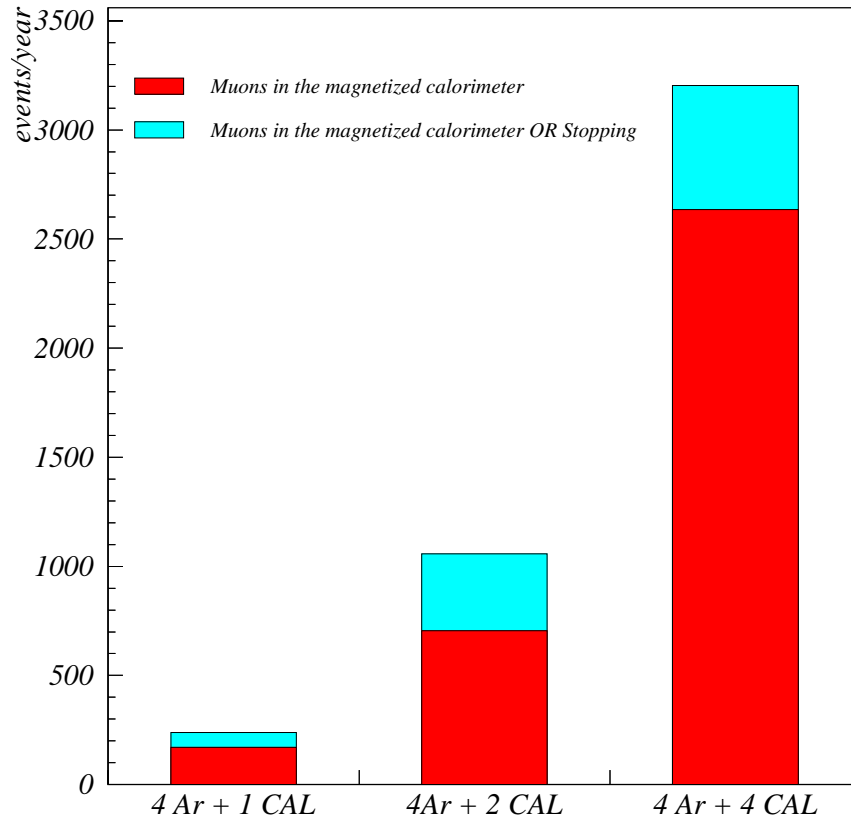
Figure 2.5: Expected statistics of ν_μCC reconstructed events with vertex in the solid target, for the three simulated detector configurations
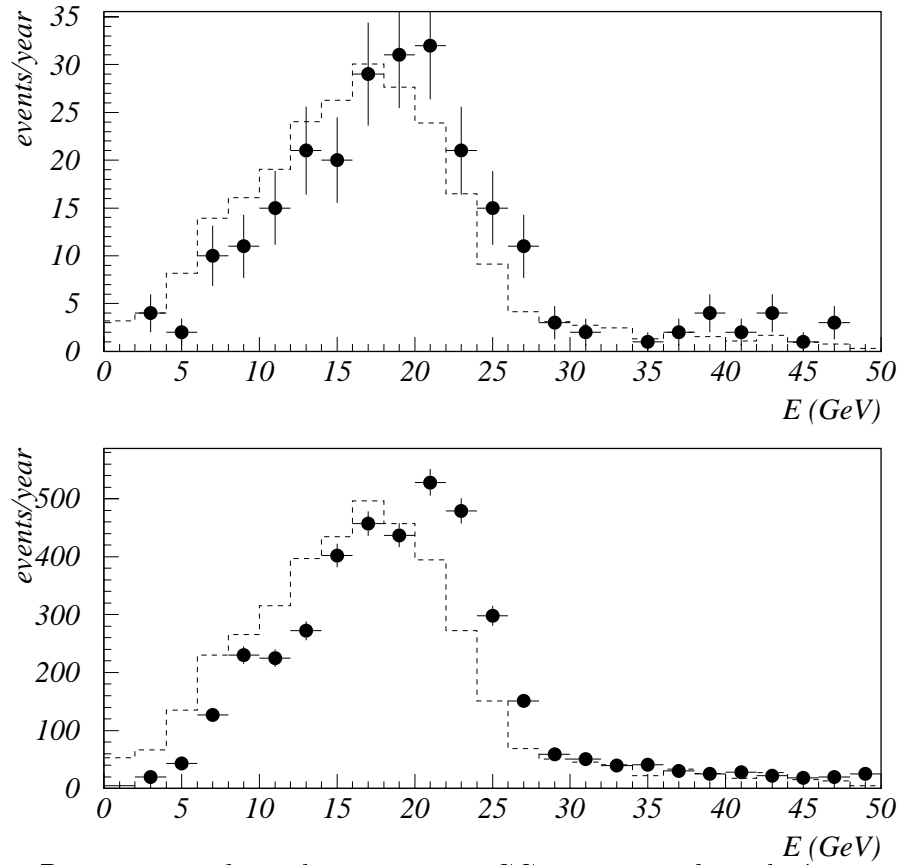
Figure 2.6: Reconstructed total energy in ν_μCC events in the calorimeter (solid points) and uncorrected energy deposition in LAr (dotted histogram), obtained with four LAr modules and one calorimeter (top) and four LAr modules and four calorimeters (bottom)
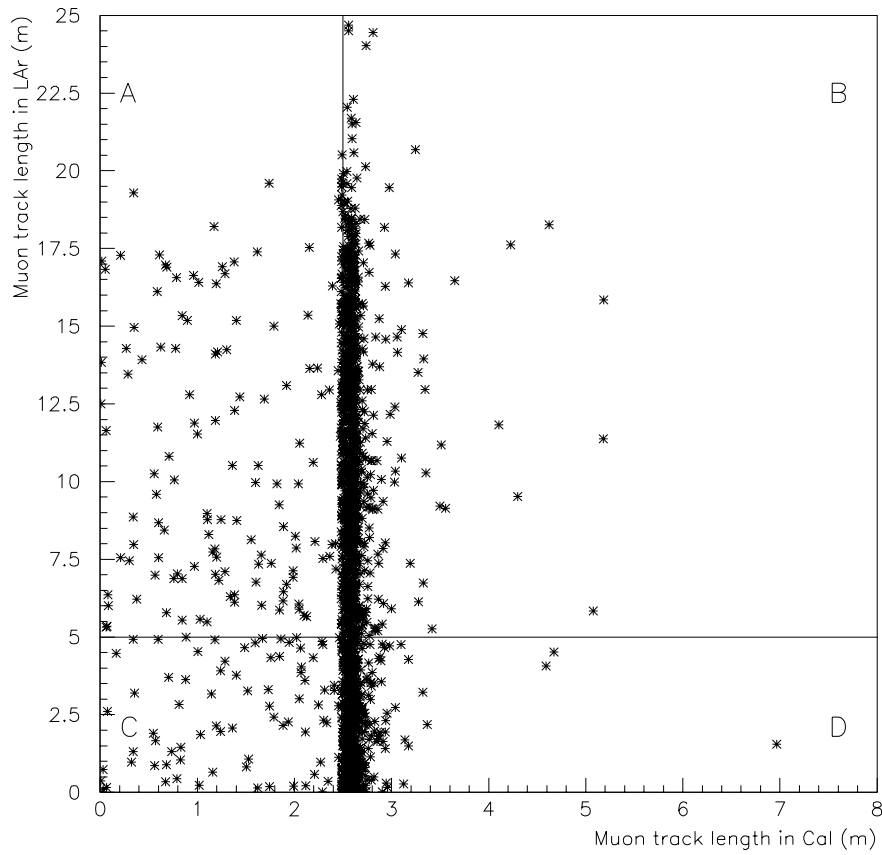
Figure 2.7: Beam neutrinos - Muon track length in LAr versus μ track length in the calorimeter for ν_μ CC transition events. The sectors A, B, C and D indicate regions in which different methods can be used to measure the muon energy (see text).

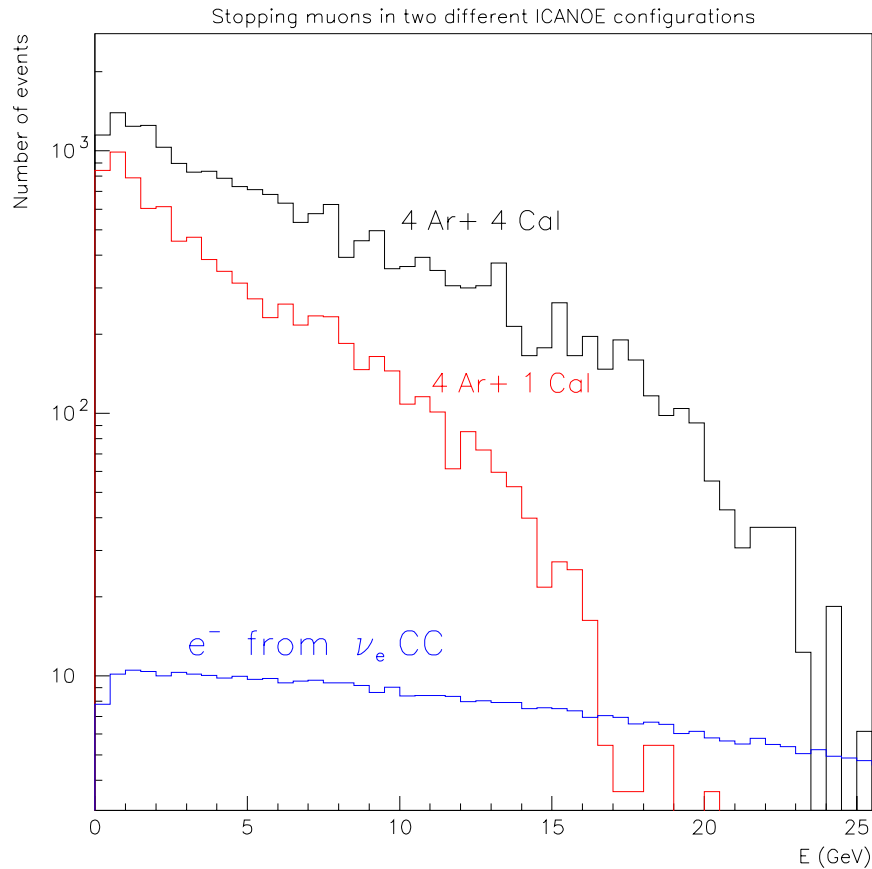## 2.2   Contribution of the solid target to signal sensitivity

Figure 2.8: Stopping muon energy distribution obtained with 4 LAr + 1 Cal and 4 LAr + 4 Cal, compared with the electron spectrum from ν_e CC : a data simulator based on the 4 LAr + 4 Cal fully covers the ν_e CC background energy spectrum.

2.2.1   Kinematical calibration and background measurement

The understanding of background events is of fundamental importance in the search for neutrino oscillation. In particular, in the ν_τ appearance analysis performed in ICANOE, the contamination of ν_e CC events, which are the main source of background, is rejected by applying a set of subsequent kinematical cuts. Therefore, the kinematics of the events need to be completely known in order to calibrate and tune the kinematical cuts leading to the selection of ν_τ events and reliably estimate the remaining background. The NOMAD experience shows that background estimates based on kinematical criteria are very demanding on the reliability of the model used to describe neutrino interactions. Despite of the improvements in the interaction modeling shown in chapter 5 of the ICANOE proposal, an independent experimental verification will be required.

In particular, the "data simulator" technique, which has been extensively used by the NOMAD Collaboration [7], relies on a simulated ν_e CC data sample, obtained by using real ν_μ CC events in which the muon is substituted with an electron. A prerequisite to successfully apply this method is to perform the muon momentum measurement with a precision comparable with that obtained for electrons. In ICANOE this method can therefore be applied only to ν_μ CC events in which the muon stops inside the detector and the muon momentum is reconstructed through range measurement.

The implementation of four calorimeters in ICANOE, increasing the total detector mass, has two benefits:

- the statistical sample of stopping muons in ν_μ CC events is enlarged

- As can be seen in Fig. 2.8, the addition of the solid target allows to extend the muon energy interval measured by range in such a way to cover with good statistics the whole region where ν_e CC events represent a potential background.

2.2.2   Search for $\nu_\mu \rightarrow \nu_\tau$ appearance in the "transition" region

Methods for ν_τ appearance search, as reported in the ICANOE Proposal [1], are based on the events occurring in the liquid target only.

In this section we extend the analysis to ν_τ charged current events occurring in the "transition" region. This region, as reported in the ICANOE proposal, corresponds to the last three meters of the liquid target of the ICANOE detector, since events with the interaction vertex localised in this region are most likely to deposit energy in both liquid and solid targets.

The channel of τ, from ν_τ interaction, decaying into an electron plus two neutrinos, which provides the best sample for ν_τ appearance studies, has been considered, assuming an exposure of 20 kton × year. The detector response has been simulated assuming a 4 super-modules configuration of the ICANOE detector. The same analysis procedure described in the ICANOE proposal has been applied to events occurring in the "transition" region, for which informations coming from the liquid and the solid targets need to be properly combined. As shown in Fig. 2.1 b) the combination of the two contributions is able to provide a proper reconstructed hadronic energy.

The calorimeter contribution is not restricted to complement the argon in energy reconstruction: Fig. 2.9 shows the reconstruction capabilities of the hadronic transverse momentum a) for events fully contained in the liquid argon volume, b) for events in the "transition" region, reconstructed by using only argon data, c)for events in the "transition" region reconstructed with the addition of the calorimetric information from the solid target, and d) by exploiting the full calorimetric + topological reconstruction in the solid target. The combined resolution appears to be still adequate to search for the tau appearance signal as discussed below.

As input parameter in the present analysis we assumed the "best" value of Δm^2 taken from the SK atmospheric neutrino data analysis, i.e. $\Delta m^2 = 3.5 \times 10^{-3} eV^2$. The corresponding rate of ν_τ CC events with $\tau \rightarrow e$ in the "transition" region is of about 21 events. The main background to this channel comes from genuine leading electrons from
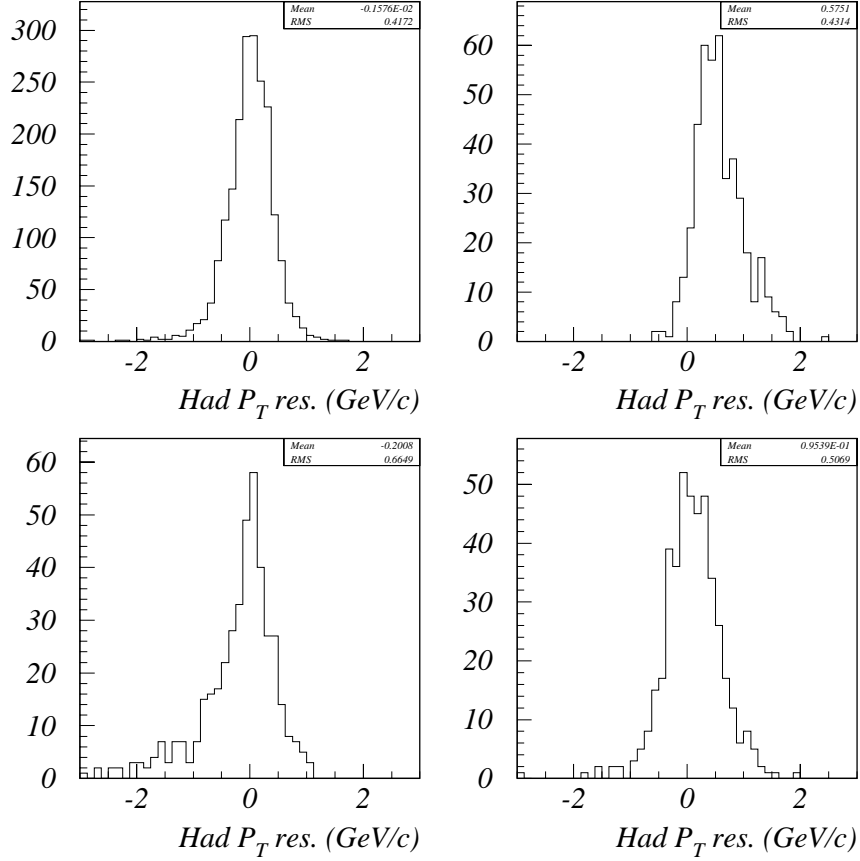
Figure 2.9: Hadronic transverse momentum reconstruction (see text)

CC interactions of the ν_e and $\bar{\nu}_e$ components of the beam. In the "transition" region these contaminations amount to ~ 80 and 5 events respectively.

A set of sequential cuts, defined in section 5.5.1 of the ICANOE proposal for the the background reduction in the liquid region, has been applied. These cuts take advantage from: (1) the softer energy spectrum for the oscillated ν_τ CC events with respect to the of ν_e CC (as reported in Fig.2.10), (2) the reduced isolation of the electron resulting from τ decay compared to the prompt electrons emerging from ν_e CC interaction, characterized by larger transverse momentum with respect to the incoming neutrino direction, as shown in Fig.2.11, (3) the harder distribution of the transverse missing momentum, in the plane perpendicular to the incoming neutrino direction, P_T^{miss}, from ν_τ interaction compared to the ν_e background, as shown in Fig.2.12.

In Table 2.1 we summarize the list of these cuts used to reduce the ν_e CC background and the expected number of signal events in the "transition" region. A τ selection efficiency of the order of 30 % is effectively reached after cuts. The $\bar{\nu}_e$ residual background contamination after cuts is negligible and it is not reported in Table 2.1.

As reported in table 5.8 of the ICANOE proposal the background contribution from νNC events is mainly reduced by the final cut exploiting the imaging capabilities and dE/dx measurements in the liquid argon. The same selections can be applied in the case of the "transition" events and reduce this source of background to a negligible level without additional loss of τ detection efficiency.
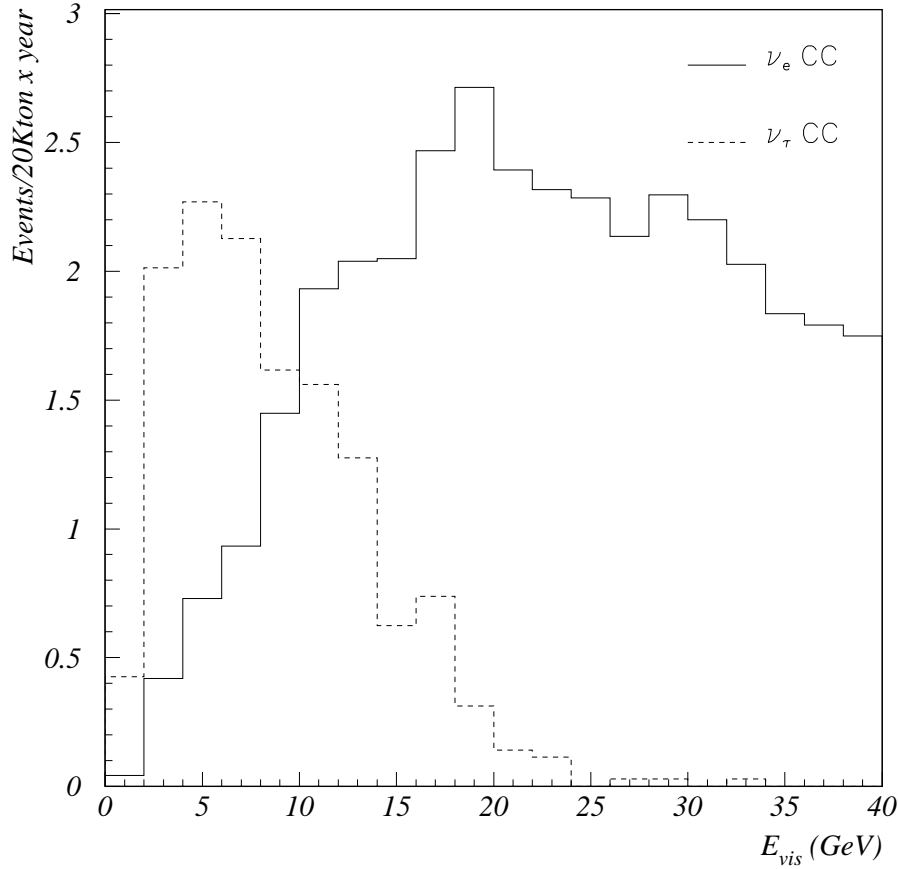
Figure 2.10: Visible energy of events for ν_e CC and ν_{tau} CC with subsequent $\tau \to e$ decay in the transition region. Curves are normalized to 20 Kton $\times$ year.

The analysis of the hadronic τ decay channels is in progress.

2.2.3   Atmospheric neutrinos

The 3-dimensional atmospheric neutrino flux [4] has been used in order to study the performance of the solid part of the ICANOE detector in the measurement of the atmospheric neutrino events. For each type of neutrino reaction and of nuclear target (i.e. Ar and Fe) 10,000 events have been generated. The detector response has been simulated assuming the design of the ICANOE proposal [1] with 4 modules. Neutrinos with $E_\nu > 500\ MeV$ have been selected in order to focus on the response of the magnetized calorimeter. The following trigger conditions have been required :

1. CAL - at least 5 digits from scintillating fibers (SCIFI) and at least 1 MeV of deposited energy in SCIFI

2. LAr - at least 50 MeV of deposited energy in the active volume of liquid argon

The main contributions of the addition of the CAL modules are:

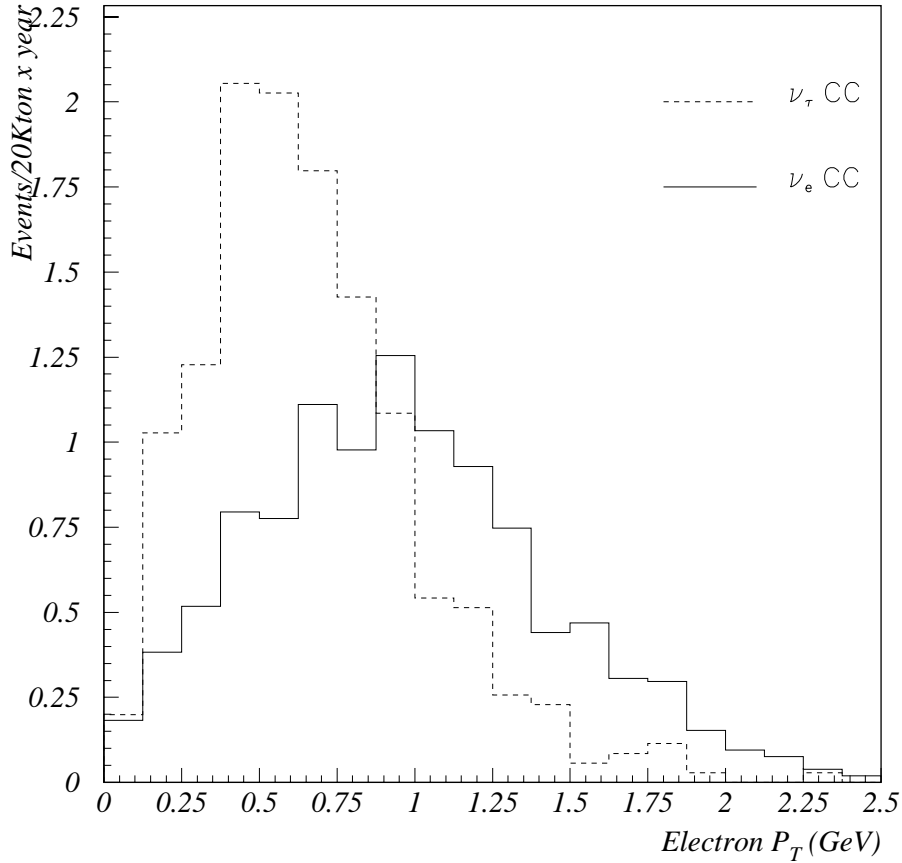- increase of the total number of events

Figure 2.11: Transverse momentum of electrons for ν_e CC and ν_{tau} CC with subsequent $\tau \to e$ decay in the transition region. Curves are normalized to 20 Kton $\times$ year.

- increase of event containment

- muon energy measurement and sign discrimination.

Increasing statistics and containment

In Tab.s 2.2 and 2.3 the expected numbers[2] of neutrino events are reported, assuming geometric or energetic containment criteria respectively defined as follows:

- **Geometric containment** - the distance between the hits and the external sensitive walls is larger than 10 cm,

- **Energetic containment** - at least 80 % of the neutrino energy is deposited in the detector (see Fig. 2.13).

The total increase in the number of contained events, due to the addition of the CAL mass, is ~ 50 %. The precise estimate of such increase shall require a more detailed study of the efficiency of reconstruction algorithms and of the background rejection. Anyway

---

[2]The expected rates for LAr events are not directly comparable with those of the proposal [1] because of the different requirements used here ($E_\nu > 500\ MeV$ and so on).
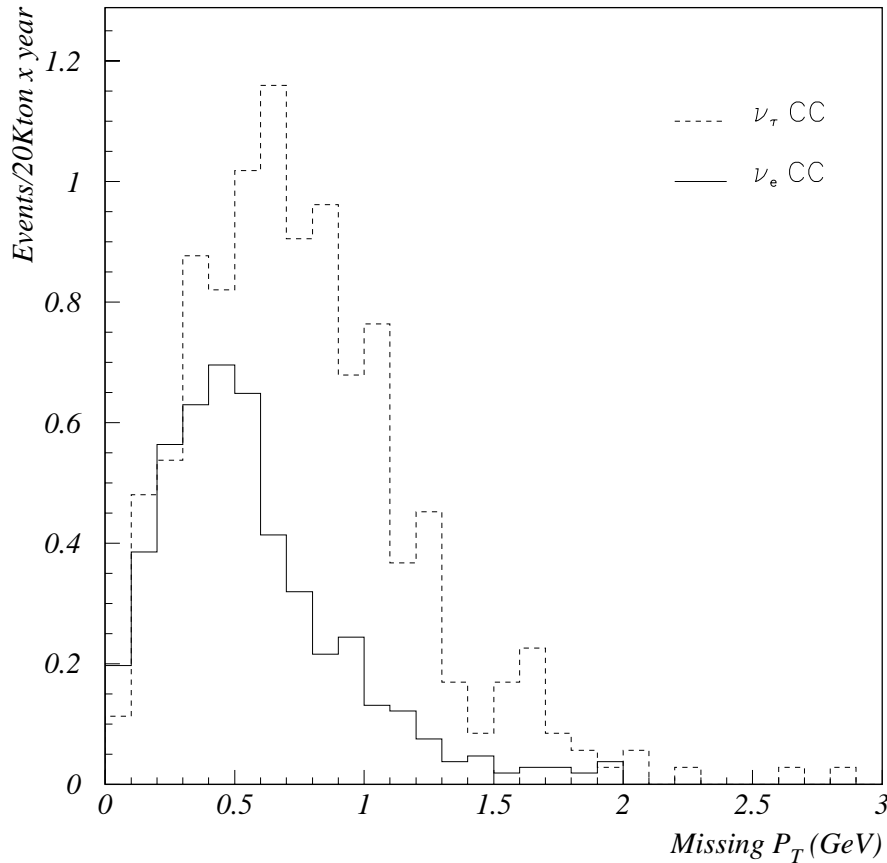
Figure 2.12: Missing total transverse momentum for ν_e CC and ν_{tau} CC with subsequent $\tau \to e$ decay in the transition region. Curves are normalized to 20 Kton × year.

these events will be available for angular analysis, ratio of no-μ/μ events measurement and so on. As an example, in Fig. 2.14 the angular distribution of μ tracks is shown with the distortion due to neutrino oscillation assuming a two-family model ($\nu_\mu \to \nu_\tau$ with maximum mixing and $\Delta m^2 = 0.005 \ eV^2$).

The fraction of events which trigger both systems (LAr and CAL) is essentially due to the shape of the energy spectrum of the atmospheric ν flux. In Tab. 2.4 we report such fractions for events with vertex in LAr and in CAL. The increase of the detector containment due to this class of events can be estimated from the comparison of the third column of Tab. 2.3 with the first and second ones.

Hadronic energy containment

The hadron energy containment is shown in Fig. 2.17 for all events (without any cut on E_ν). The high density of the calorimeter allows to reach a good containment despite the geometrical dimensions : more than 50 % of the events with $E_\nu > 500 \ MeV$ deposit in the CAL modules more than 60 % of the energy of the hadronic jet. Therefore, once the muon has been measured, the relevant parameter is the containment of the hadronic jet.

Cuts	ν_τ Eff. (%)	ν_e CC	ν_τ CC $\Delta m^2 = 3.5 \times 10^{-3} eV^2$
Initial	100	80	21
Fiducial volume	79	62	16
One candidate with momentum > 1 GeV	64	59	13
$E_{vis} < 18$ GeV	61	11	12
$p_T^e < 0.9$ GeV	49	4.9	10
$p_T^{miss} > 0.6$ GeV	30	1.7	6.3

Table 2.1: Rejection of the ν_e CC background in the $\tau \to e$ analysis. Figures are normalized to an exposition of 20 Kton $\times$ year

	whole detector contained events	average $E_\nu(GeV)$
ν_e CC in CAL	215	2.0
$\bar{\nu}_e$ CC in CAL	58	2.5
ν_μ CC in CAL	406	1.7
$\bar{\nu}_\mu$ CC in CAL	115	1.8
NC in CAL	181	3.2
ν_e CC in LAr	361	1.4
$\bar{\nu}_e$ CC in LAr	79	1.9
ν_μ CC in LAr	569	1.2
$\bar{\nu}_\mu$ CC in LAr	162	1.2
NC in LAr	456	2.3

Table 2.2: Atmospheric neutrinos - Geometrically contained events characterized by the vertex location. Four years of data taking and four modules are assumed. Each module has a mass of 2.3 *kton* (1.4 *kton* for LAr, 0.7 *kton* for CAL).

Muon energy measurement for LAr $\to$ CAL events

The containment of ν_μ and $\bar{\nu}_\mu$ CC events is worse because of the escaping lepton. In Fig.s 2.15, 2.16 and 2.18 the containment is shown for atmospheric neutrino events.

Therefore the muon energy measurement results crucial and the methods discussed in Sec.2.1.4 are used.

In Fig. 2.19 we show the muon track lengths in both the subdetectors for ν_μ CC LAr $\to$ CAL beam events. The plot has been divided in four regions assuming 1.5 m as a minimum length needed for the magnetic reconstruction and 3 m for the MS method[3].

With these values, in 4 years of data taking we expect 117 $\nu_\mu + \bar{\nu}_\mu$ atmospheric events in region A, 111 in region B, 203 in region C, 115 in region D. In region C $\sim$ 70 % of

---

[3]The threshold values are different from those used in Fig. 2.7 due to the lower energies of muons. The values here used are just indicative.
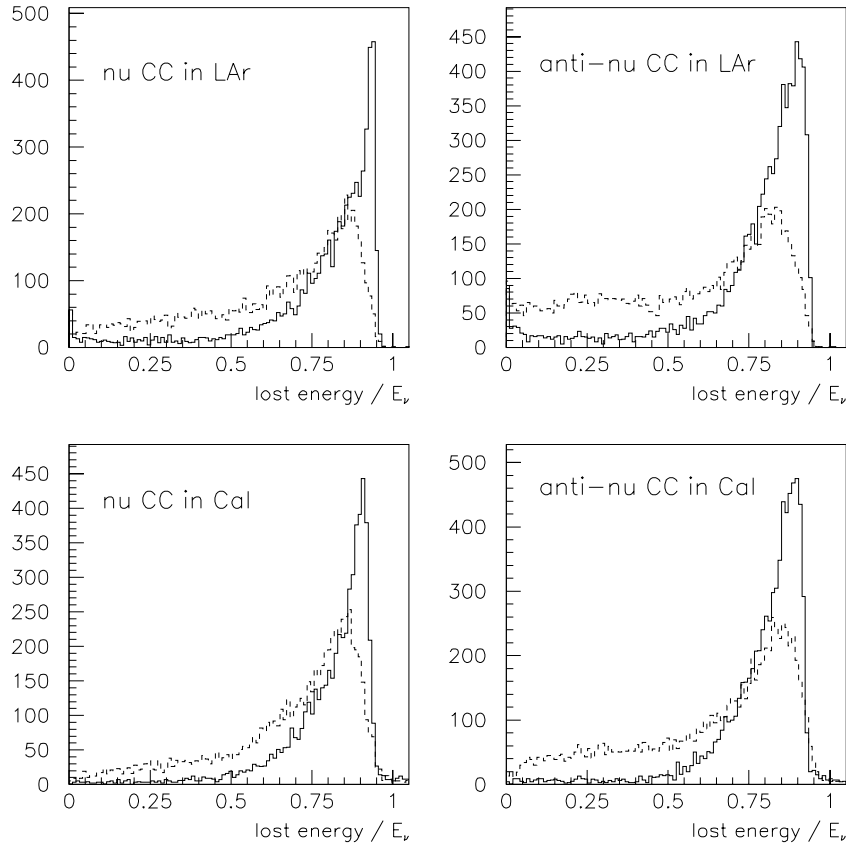
Figure 2.13: Atmospheric neutrinos - Fraction of energy deposited (uncorrected) in the detector for different types of ν CC reactions with vertex in LAr or in CAL. The solid and dashed histograms refer to ν_e and ν_μ interactions respectively. No account has been made of the escaping muon energy measurement using the magnet or the multiple scattering technique.

muons stop in the calorimeter and the momentum is measured by the *range* method.
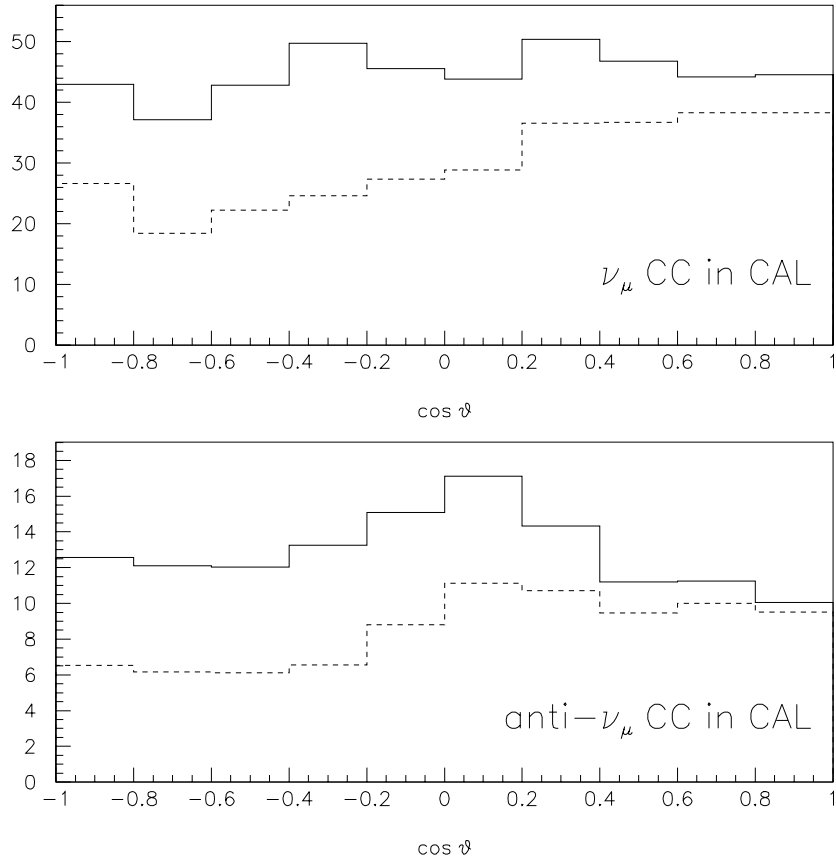
Figure 2.14: Atmospheric neutrinos - Angular distribution of muon tracks due to energetically contained ν_μ CC events with the vertex in CAL. Four years of data taking and four modules are assumed. The dashed line indicates the distribution assuming $\nu_\mu \to \nu_\tau$ oscillation with maximum mixing and $\Delta m^2 = 0.005 \; eV^2$.

	contained events in CAL	contained events in LAr	whole detector contained events	average $E_\nu (GeV)$
ν_e CC in CAL	290	–	301	2.3
$\bar{\nu}_e$ CC in CAL	82	–	85	3.4
ν_μ CC in CAL	387	–	448 (298)	1.8
$\bar{\nu}_\mu$ CC in CAL	106	–	129 (85)	1.9
ν_e CC in LAr	–	571	594	2.4
$\bar{\nu}_e$ CC in LAr	–	135	141	3.3
ν_μ CC in LAr	–	592	671 (448)	1.6
$\bar{\nu}_\mu$ CC in LAr	–	150	178 (122)	1.7

Table 2.3: Atmospheric neutrinos - Energetically contained events characterized by the vertex location. In parenthesis the number of expected events assuming a two-family oscillation model ($\nu_\mu \to \nu_\tau$ with maximal mixing and $\Delta m^2 = 0.005 \; eV^2$).
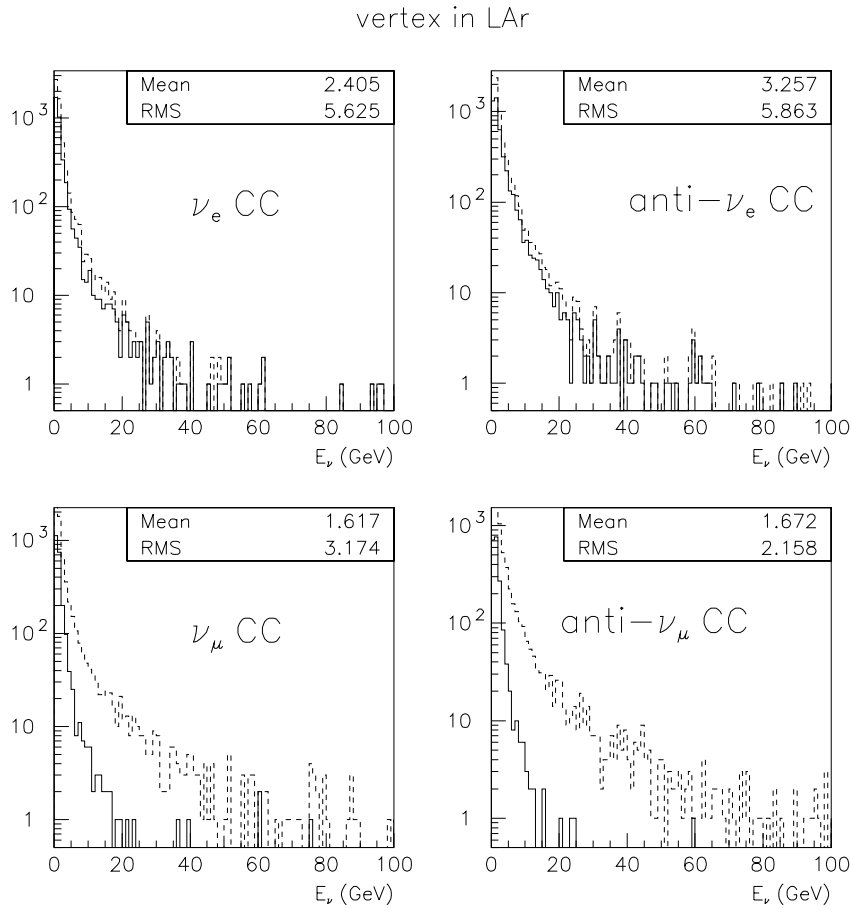
vertex in LAr

Figure 2.15: Atmospheric neutrinos - Neutrino energy distributions for CC events with vertex in LAr. For the dashed histograms only the trigger condition is required, while solid histograms refer to *energetically* contained events in ICANOE (see text). The mean and the RMS values refer to the contained events.

	vertex in CAL	vertex in LAr
ν_e CC	6 %	6 %
$\bar{\nu}_e$ CC	6 %	7 %
ν_μ CC	16 %	10 %
$\bar{\nu}_\mu$ CC	19 %	11 %
NC	5 %	6 %

Table 2.4: Atmospheric neutrinos - Percentage of events with trigger in both subdetectors with respect to the number of events with vertex in LAr and CAL respectively.
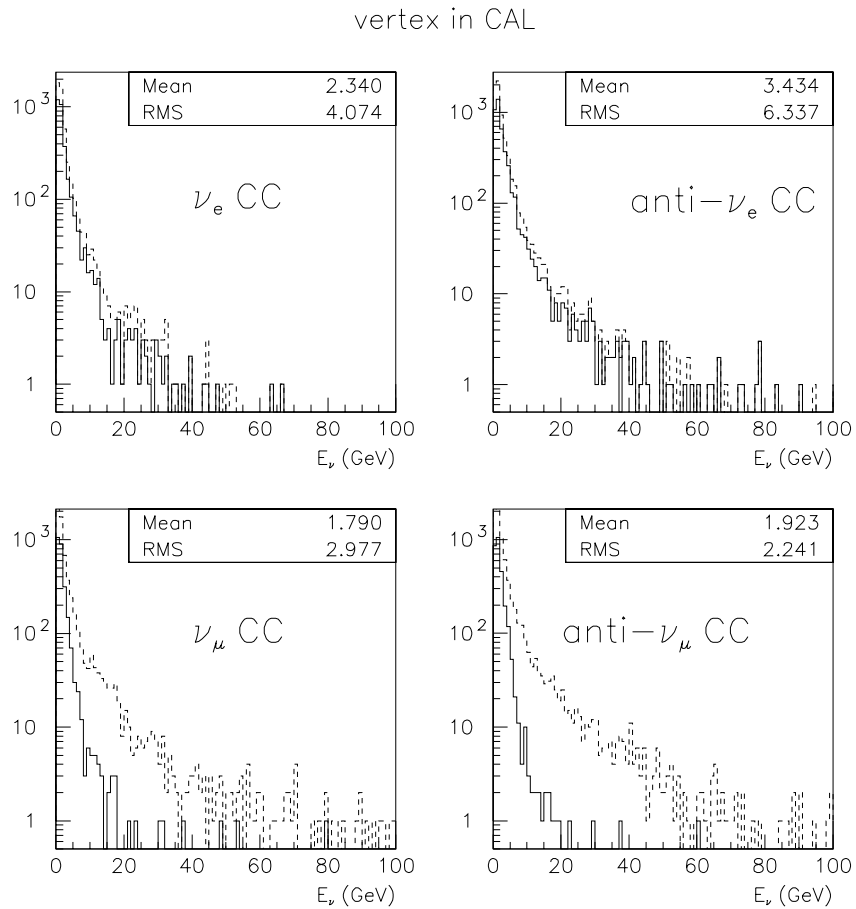
Figure 2.16: Atmospheric neutrinos - Same of Fig. 2.15 but for events with vertex in CAL.
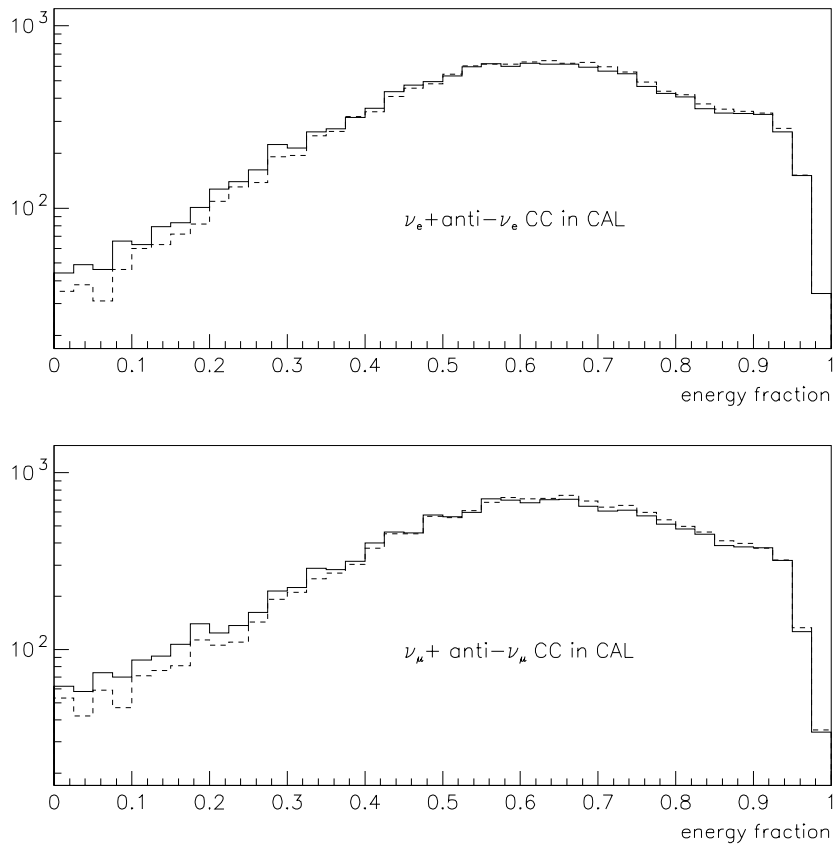
Figure 2.17: Atmospheric neutrinos - Fraction of uncorrected hadron jet energy deposited in the detector. The full line refers to the calorimeter, the dashed line to the whole detector.
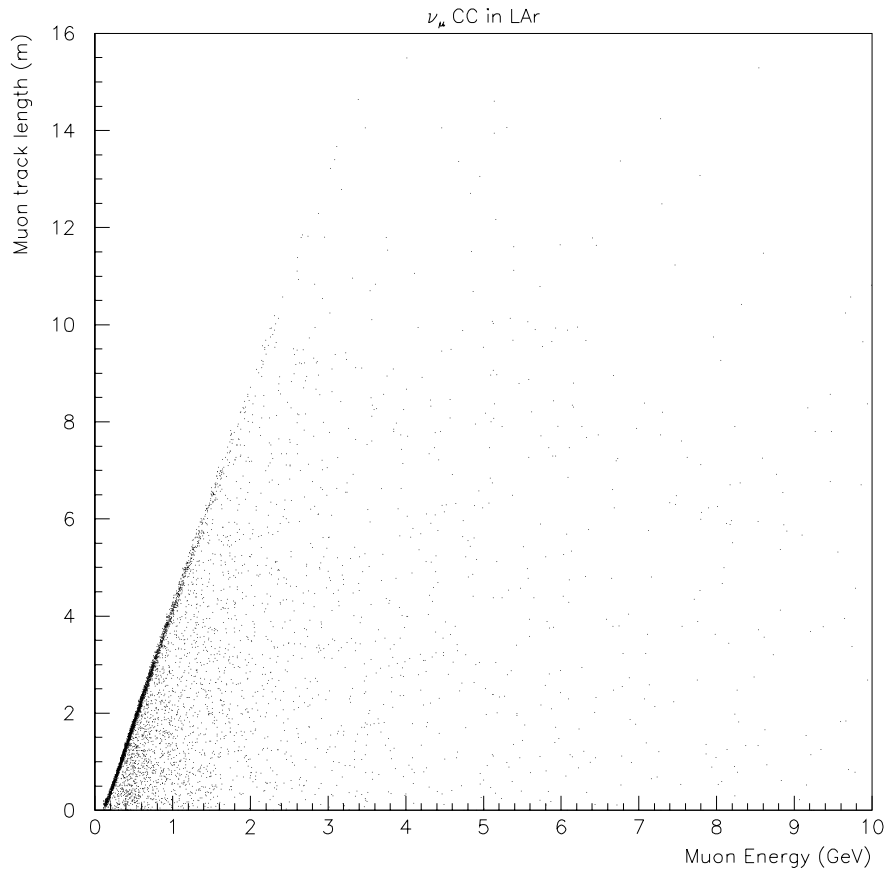
Figure 2.18: Atmospheric neutrinos - Muon track length in LAr versus μ energy for ν_μ CC interactions with vertex in LAr. The line with larger dot density is due to events which are fully contained in LAr.
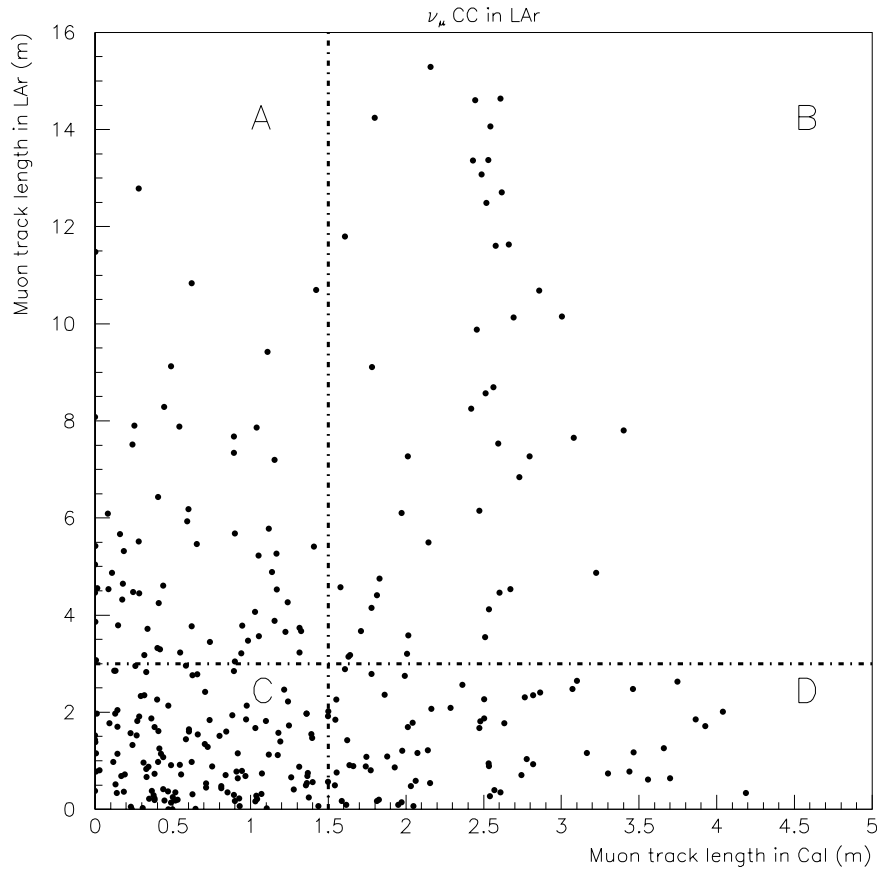
Figure 2.19: Atmospheric neutrinos - Muon track length in LAr versus μ track length in CAL for ν_μ CC LAr $\rightarrow$ CAL events. The sectors A, B, C and D indicate regions in which different methods can be used to measure the muon energy (see text).

Chapter 3

Beam systematics

The ν_e contamination of the CNGS beam is relevant for both the $\nu_\mu \rightarrow \nu_\tau$ and $\nu_\mu \rightarrow \nu_e$ channel. In the latter case the statistical fluctuations in the ν_e background are the irreducible limiting factor. For an integrated exposure of 20 kTon $\times$ yr at CNGS, the expected number of $\nu_e + \overline{\nu}_e$ CC interactions in the LAr target is 455 and the corresponding statistical error is $\approx 5\%$. The systematics associated with the ν_e contamination are connected with:

1. The ability to calculate the correct neutrino fluence and spectral shape for a given target/focusing system/decay tunnel configuration

2. The possible errors and/or lack of reproducibility in the relevant setup parameters, i.e.:

   - Beam emittance, particularly beam shape and possible tails
   - Beam centering on the target
   - Relative alignment errors in the target/horn/reflector system
   - Ripples/offset in the horn/reflector current pulses
   - Absolute alignment errors with respect to the Gran Sasso site

A preliminary indication about the achievable accuracy can be derived from the experience of the present WANF beam. The main difference between CNGS and WANF is of course the statistics in the total number of events, but within the limits due to the reduced statistics, the systematic error of WANF sets the scale of the problem. The uncertainties in pion and kaon production should affect CNGS and WANF in a similar way, with perhaps less impact on CNGS due to the larger angular acceptance of the focusing system ($\approx$ 20 mrad instead of $\approx$ 10 mrad). The use of the latest experimental results from SPY [5], together with updated models for beam interactions [6], results in a 5-7% systematic level at WANF [7]. Furthermore, as it will be shown in the following, the uncertainties in kaon production (which are the main source of the ν_e component) can be reduced using the experimental information of high energy part of the ν_μ which originates from the same parent particles.

The influence of some of the instrumental effects has been investigated simulating the CNGS beam both with the nominal setup ("CNGS" beam in the following) and with

Figure 3.1: ν_μ CC spectra for the nominal CNGS beam, for the same beam assuming a misalignment of 400 m of the beam axis at Gran Sasso ("CNGS-1") and for a beam with several inaccuracies as described in the text ("CNGS-2"). The error bars represent the statistical errors after an exposure of 20 kTon×yr.
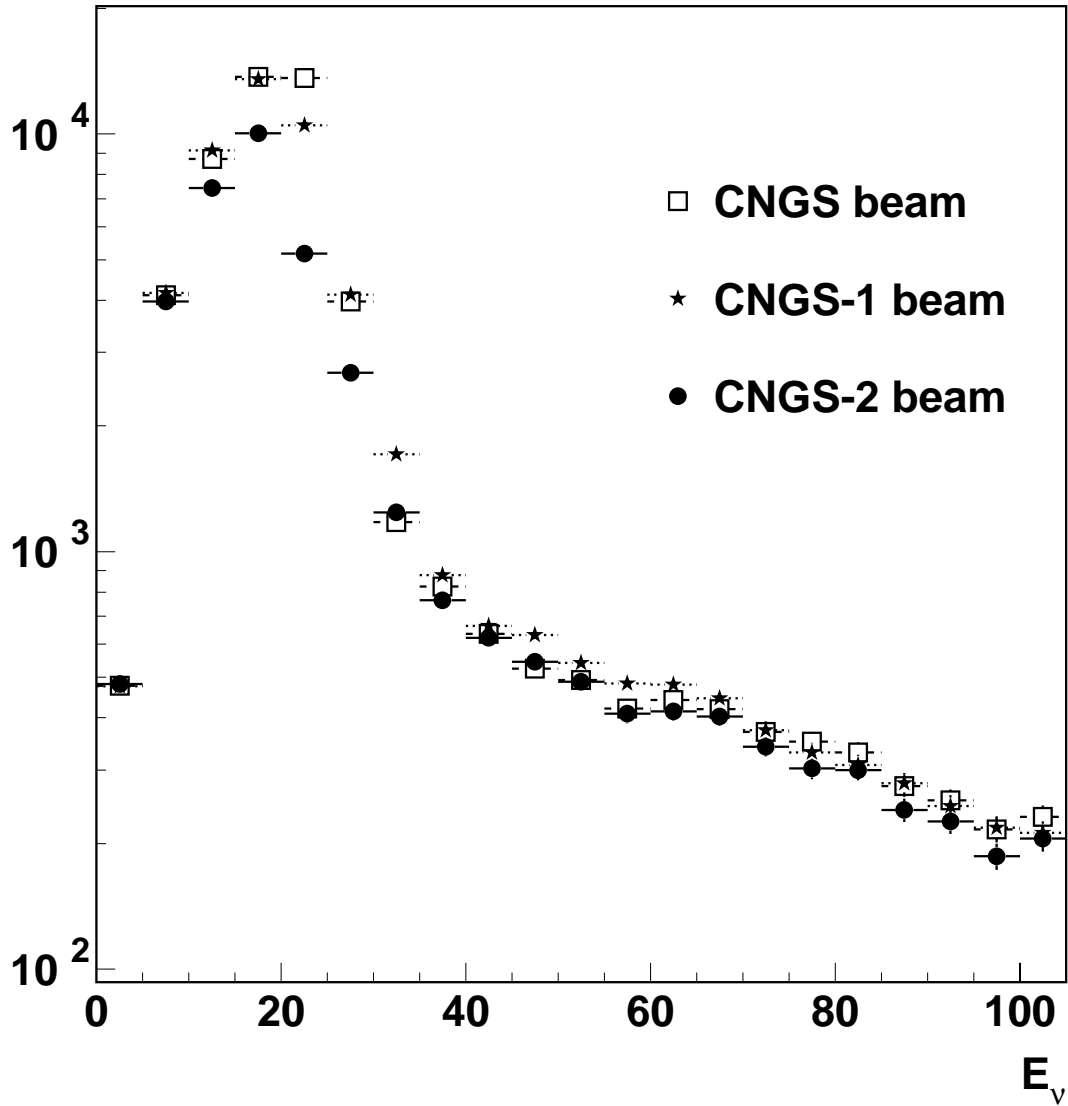
Figure 3.2: ν_e CC spectra for the nominal CNGS beam and for the same beam assuming a misalignment of 400 m of the beam axis at Gran Sasso ("CNGS-1"). The ν_e spectra have been multiplied by a factor 40 and are superimposed to the corresponding ν_μ CC spectra. The error bars represent the statistical errors after an exposure of 20 kTon×yr.
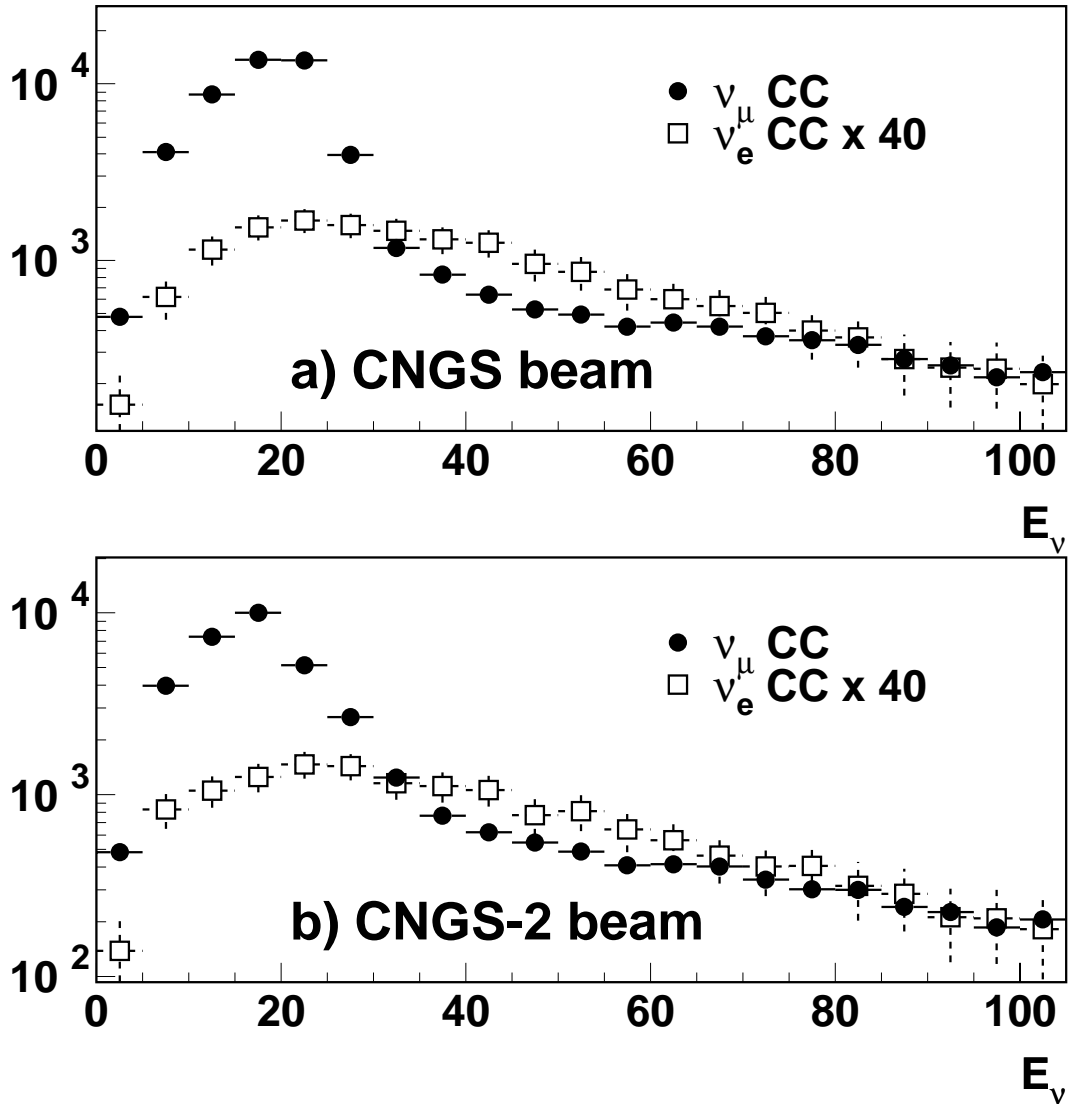
Figure 3.3: ν_e CC spectra for the nominal CNGS beam and and for a beam with several inaccuracies as described in the text ("CNGS-2"). The ν_e spectra have been multiplied by a factor 40 and are superimposed to the corresponding ν_μ CC spectra. The error bars represent the statistical errors after an exposure of 20 kTon×yr.
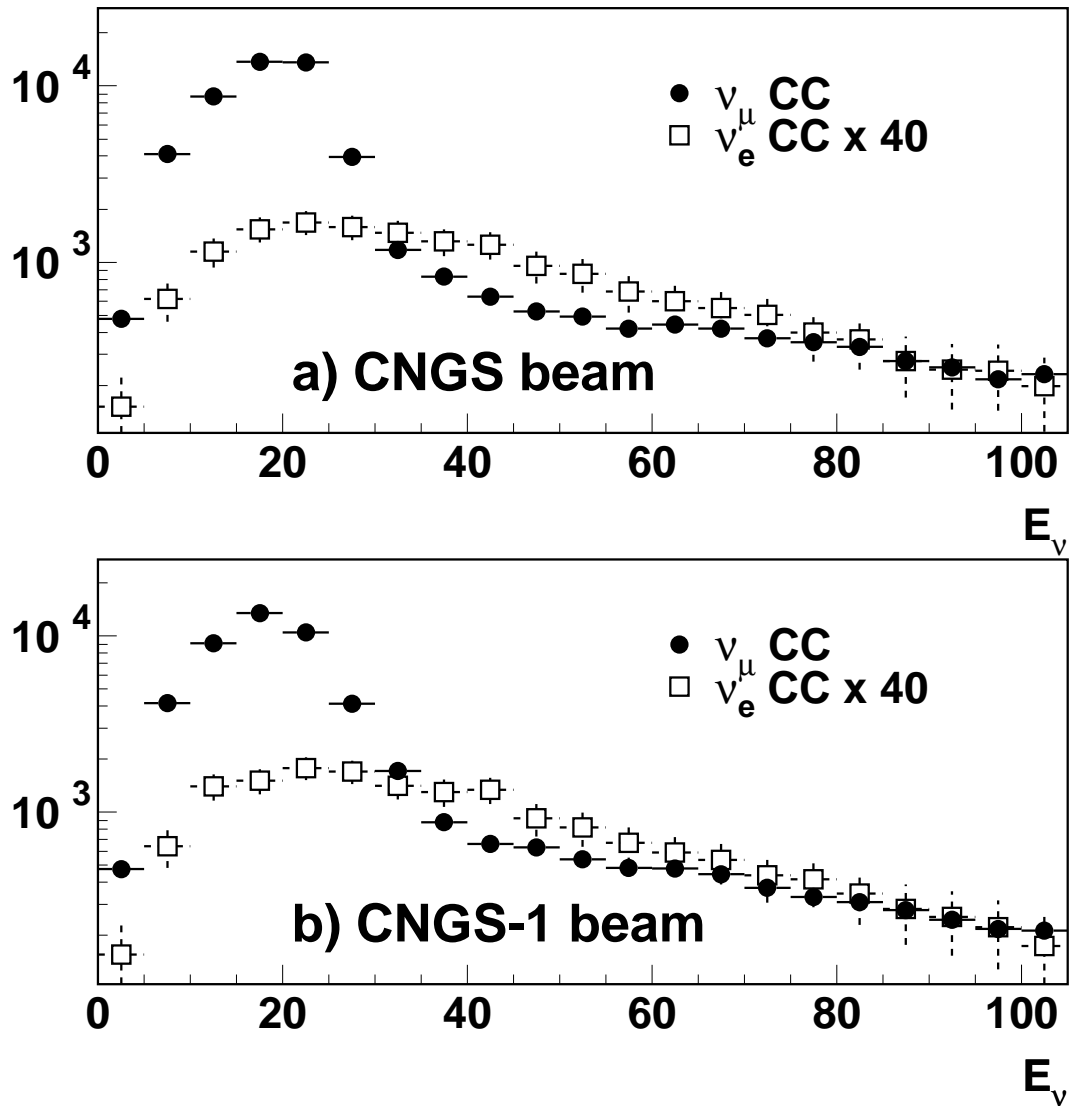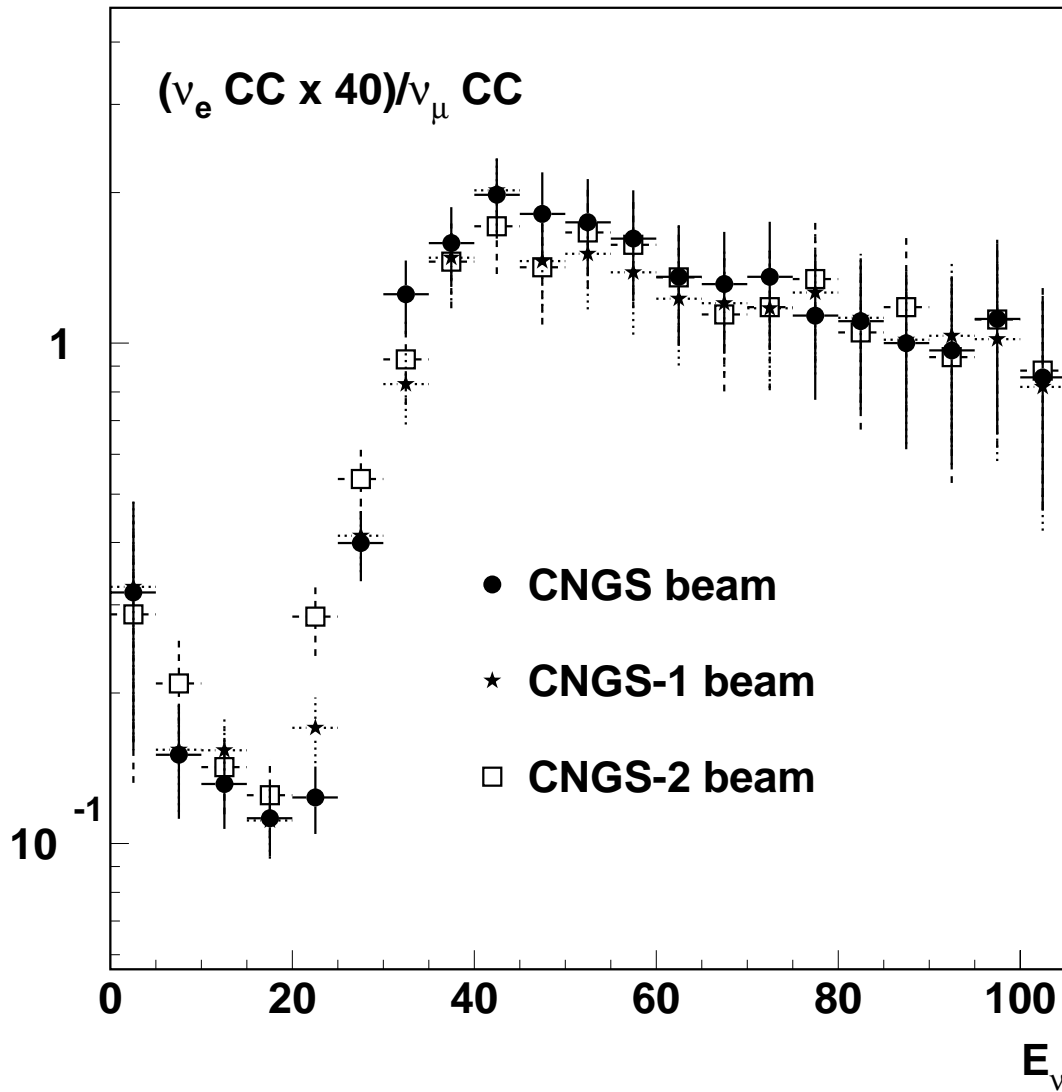
Figure 3.4: Ratio ν_e CC over ν_μ CC as a function of the neutrino energy, for the nominal CNGS beam, for the same beam assuming a misalignment of 400 m of the beam axis at Gran Sasso ("CNGS-1"), and for a beam with several inaccuracies as described in the text ("CNGS-2"). The ν_e rates have been multiplied by a factor 40 in such a way to bring the ratio close to one at high energies. The error bars represent the statistical errors after an exposure of 20 kTon×yr.

	All Energies		E $\geq$ 60 GeV	
Beam	ν_μ	$\nu_e + \overline{\nu}_e$	ν_μ	$\nu_e + \overline{\nu}_e$
CNGS	54300	455	4844	118
CNGS-1	52319	462	4775	115
CNGS-2	38645	408	4301	110

Table 3.1: Expected events rates of ν_μ and $\nu_e + \overline{\nu}_e$ for an integrated exposure of 20 kton×years for different beam simulations.

	All Energies	E $\geq$ 60 GeV
Beam	$(\nu_e + \overline{\nu}_e)/\nu_\mu$	$(\nu_e + \overline{\nu}_e)/\nu_\mu$
CNGS	$0.84 \cdot 10^{-2}$	0.024
CNGS-1	$0.87 \cdot 10^{-2}$	0.024
CNGS-2	$1.06 \cdot 10^{-2}$	0.026

Table 3.2: Ratio of $\nu_e + \overline{\nu}_e$ over ν_μ event rates expected for an integrated exposure of 20 kton×year for different beam simulations.

a setup ("CNGS-1") still with the nominal beam but assuming a misalignment beam axis-detector of 400 m at the Gran Sasso location (which corresponds to ≈ 0.6 mrad).

A further setup ("CNGS-2") where some of the critical parameters have been varied by some amount has been investigated. In particular:

1. The beam impact position has been assumed out of 1 mm with respect to the target rod axis

2. The reflector and horn positions have been radially offset of 2 cm with respect to the target axis

3. 10 % of the beam particles are distributed with a sigma three times larger than the nominal one, in order to simulate non gaussian tails in the beam shape

4. The horn and reflector peak currents have been lowered of 10 % with respect to the nominal values

All the "errors" listed above are unreasonably large. They have been chosen in order to see a detectable effect on the various beam components and to illustrate how even such extreme values do not influence in a dramatic way the beam characteristics, particularly the ν_e contamination.

The ν_μ and $\nu_e + \overline{\nu}_e$ ("ν_e" from now on) CC rates are presented in table 3.1 for the three configurations. The ratios ν_e/ν_μ are given in table 3.2.

The CC ν_μ event spectra for CNGS, CNGS-1 and CNGS-2 are presented in figure 3.1. The ν_μ rates in the region of the main peak are subject to significant variations, while the high energy region is much less sensitive to the adopted variation in the beam setup. According to these results, it seems that a 30 % bin-to-bin systematic error in the ν_μ CC

spectrum is a conservative estimate, which is likely to be overestimated for reasonable values of the systematics associated with the beam.

The ν_e CC spectra for the various beam configurations are presented in figures 3.2,3.3 compared with the ν_μ CC spectra. The ratios between ν_e and ν_μ are presented in figure 3.4.

The ν_e contamination is fairly less sensitive to the investigated variations in the beam setup. This is an expected result since ν_e's come mostly from kaon decays, where the large available phase space and the three body final state makes the correlation between the neutrino and hadron energy weaker than for pion decays. Furthermore, the larger decay p_t favors high energy kaons for solid angle considerations, which are less sensitive to the focusing details and produces a wider angular distribution. As expected, similar remarks apply to the high energy component of the ν_μ spectra which also originates from kaon decays. The results presented in figure 3.4 and in tables 3.1,3.2 show that the ν_e contamination can be accurately estimated both in absolute value and shape, from the (measured) ν_μ high energy component with a comfortably low statistical error. The adopted 10 % systematic error is again conservative, since under the extreme conditions used for the beam systematics the variations in the ν_e contamination are within this limit when normalized to the high energy ν_μ component, and only slightly larger when using the whole ν_μ spectrum.

Chapter 4

Determination of the oscillation parameters

4.1 Three neutrino mixing scenario

The indication for the existence of neutrino oscillations has been strongly supported by the recent SuperKamiokande data. If neutrino oscillations are indeed the cause of the effects seen in the atmospheric neutrino experiments, the next task will clearly be to measure with great accuracy the oscillation parameters.

ICANOE can provide very powerful answers to this question. First of all, it can study *both* beam neutrinos and atmospheric neutrinos with unprecedented resolution, providing truly complementary information on the oscillation mechanisms. Secondly, in order to fully sort out the mixing matrix, unambiguous neutrino flavor identification is mandatory to distinguish τ's from ν_τ's and electrons from ν_e's interactions. This is clearly provided by excellent lepton identification and full kinematical reconstruction where excellent resolution can be achieved for events occurring in the liquid target of *ICANOE*. The liquid and solid targets have each sufficient mass to accumulate muon charged current data with high statistical accuracy. Beam muon neutrino disappearance measurements can provide additional handles in the determination of the Δm_{32}^2 parameter, even in the presence of uncertainties associated to the knowledge of the unoscillated beam which is not measured by a near station.

We have studied the possibility to determine the oscillation parameters in *ICANOE* by performing a χ^2 minimization of a sample of independent observables obtainable in *ICANOE* under the hypothesis of a 3 neutrino family mixing scenario.

To be general, one must account for flavor oscillations using a 3 neutrino mixing scenario[1]. A 3×3 unitary matrix describes the mixing between flavor and mass eigenstates. With three neutrino states, oscillations will be driven by only two independent mass square differences, say $\Delta m_{32}^2 = m_3^2 - m_2^2$ and $\Delta m_{21}^2 = m_2^2 - m_1^2$. The mixing between the mass and weak eigenstates can be parametrized by the 3×3 CKM-like matrix, i.e.

---

[1]The oscillation pattern of the neutrinos may in principle be even more complicated and involve a combination of flavor and $\nu_X \to \nu_{sterile}$ transitions. Since as shown below we will assume the absolute knowledge of the ν_μ CC beam is at the level of 30% systematic error, any ν_μ disappearance to a sterile state with a probability smaller than that level is at first order negligible.

$$U = \begin{pmatrix} c_{12}c_{13} & s_{12}c_{13} & s_{13}e^{-i\delta} \\ -s_{12}c_{23} - c_{12}s_{13}s_{23}e^{i\delta} & c_{12}c_{23} - s_{12}s_{13}s_{23}e^{i\delta} & c_{13}s_{23} \\ s_{12}s_{23} - c_{12}s_{13}c_{23}e^{i\delta} & -c_{12}s_{23} - s_{12}s_{13}c_{23}e^{i\delta} & c_{13}c_{23} \end{pmatrix} \qquad (4.1)$$

but we will ignore possible effects due to the CP-phase δ.

The current experimental results on solar and atmospheric neutrinos allow us to consider the approximation that only one mass scale is relevant, since if we assign $\Delta m_{32}^2 (\Delta m_{21}^2)$ to the atmospheric(solar) oscillations, then $\Delta m_{32}^2 \gg \Delta m_{21}^2$. This implies that the two oscillations driven by the mass differences Δm_{32}^2 and Δm_{21}^2 decouple and can be studied independently.

The three-family oscillation is then described by only three parameters: the mass difference Δm_{32}^2 and the two mixing angles θ_{13} and θ_{23}. Neglecting possible matter effects, we can write the oscillations probabilities in the following form:

$$\begin{aligned} P(\nu_e \rightarrow \nu_e) &= 1 - \sin^2(2\theta_{13})\Delta_{32}^2 \\ P(\nu_e \rightarrow \nu_\mu) &= \sin^2(2\theta_{13})\sin^2(\theta_{23})\Delta_{32}^2 \\ P(\nu_e \rightarrow \nu_\tau) &= \sin^2(2\theta_{13})\cos^2(\theta_{23})\Delta_{32}^2 \\ P(\nu_\mu \rightarrow \nu_\mu) &= 1 - 4\cos^2(\theta_{13})\sin^2(\theta_{23})[1 - \cos^2(\theta_{13})\sin^2(\theta_{23})]\Delta_{32}^2 \\ P(\nu_\mu \rightarrow \nu_\tau) &= \cos^4(\theta_{13})\sin^2(2\theta_{23})\Delta_{32}^2 \\ P(\nu_\tau \rightarrow \nu_\tau) &= 1 - 4\cos^2(\theta_{13})\cos^2(\theta_{23})[1 - \cos^2(\theta_{13})\cos^2(\theta_{23})]\Delta_{32}^2 \end{aligned} \qquad (4.2)$$

where $\Delta_{32}^2 = \sin^2(1.27\Delta m_{32}^2 L/E)$ and identical expressions for anti-neutrinos.

Our task is to understand our ability to determine precisely **all the parameters** involved in these neutrino oscillations, i.e. θ_{13}, θ_{23} and Δm_{32}^2.

We decided to define the two mixing angles θ_{23} and θ_{13} in the interval $[0, \pi/4]$, which in practice, only implies that $P(\nu_e \rightarrow \nu_\tau) \leq P(\nu_e \rightarrow \nu_\mu)$, which is a reasonable assumption given the atmospheric neutrino results. The clarity of our results benefit from this since mixing angles can be expressed in terms of $\sin^2 2\theta_{13}$ and $\sin^2 2\theta_{23}$ in the interval $[0, 1]$. We could of course have decided to extend the interval to the full $[0, \pi/2]$ interval without any impact in our conclusions.

To constrain oscillation scenarios, one must couple appearance signatures in several different channels and disappearance signatures. In addition, the combination of the complementary information from the observation of the long-baseline CNGS beam and the high statistics unbiased observation of the atmospheric neutrinos of all flavors (e,mu and tau like) provide a further powerful constraint on the oscillations parameters, as we will show below.

For small values of L/E, (i.e. $E/L \gg \Delta m_{32}^2$) the oscillatory term Δ_{32}^2 can be approximated as:

$$\Delta_{32}^2 \simeq \left(\frac{1.27\Delta m_{32}^2 L}{E} \right)^2. \qquad (4.3)$$

Note that in this case, the three parameters θ_{13}, θ_{23} and Δm_{32}^2 appear as a single multiplicative factors in the expression of the oscillation probabilities and therefore angles

Process	liquid target	transition region	solid
ν_μ CC	54300	10200	27150
$\bar{\nu}_\mu$ CC	1090	200	545
ν_e CC	437	80	219
$\bar{\nu}_e$ CC	29	5	15
ν NC	17750	3330	8875
$\bar{\nu}$ NC	410	77	205

Table 4.1: Expected event rates for an exposure of 20 kton× year for the liquid target and 10 kton× year for the solid target. All the rates include nuclear corrections and are computed for the proper target composition. No oscillations are assumed.

and masses can no more be measured separately. However, the combination of the various oscillations signatures provides the necessary way to solve this problem, since it is equivalent to solving a system of more than three equations with three unknowns.

4.2 Reference oscillation parameters

The reference magnitudes are computed assuming the following values for the oscillation parameters (no CP-violation):

$$\Delta m_{32}^2 = 3.5 \times 10^{-3} \text{ eV}^2 \qquad \sin^2 2\theta_{13} = 0.1, \qquad \sin^2 2\theta_{23} = 0.9$$

These values are consistent with all available data from previous atmospheric and reactor data.

4.3 The CNGS long baseline data

Events will occur in the whole *ICANOE* detector. As reference, we assume an exposure of 20 kton × year for the liquid argon. This corresponds to four years running of the CNGS beam in shared mode. For the events occurring in the solid detector, given the smaller mass, the reference exposure is 10 kton × year. The last three meters of the liquid target are defined as a transition region, since beam events occurring in this region are most likely to deposit energy in both targets. Table 4.1 shows the computed total event rates for each neutrino species present in the beam for the liquid, solid and in the transition region.

4.4 Appearance signatures

In the CERN-NGS beam, the expected ν_e and ν_τ contamination are of the order of 10^{-2} and 10^{-7} respectively compared to the dominant ν_μ composition. These properties allow to search for oscillations by looking at the appearance of ν_e or ν_τ charged current events. In this case, the detector must be able to tag efficiently the interaction of ν_e's and ν_τ's

out of the bulk of ν_μ events. This requires a detailed event reconstruction that can be achieved only by means of a high granularity detector. This requirement was shown to be met in the *ICANOE* detector.

In order to separate ν_τ events from the background, two basic criteria, already adopted by the short baseline NOMAD experiment, can be used:

- an unbalanced total transverse momentum due to neutrinos produced in the τ decay,

- a kinematical isolation in the transverse plane.

In addition, given the baseline L between CERN and GranSasso, for the lower Δm^2_{32} values of the allowed region indicated by the atmospheric neutrino results, we expect most of the oscillation to occur at low energy. In this case, a criteria on the visible energy is also very important to suppress backgrounds.

Figure 4.1 shows the distribution of the total visible energy of the events, the transverse momentum of the electron candidate and the total missing transverse momentum in the event. The plots correspond to the oscillation scenario with $\Delta m^2_{32} = 3.5 \times 10^{-3}$ eV^2, $\sin^2 2\theta_{23} = 0.9$ and $\sin^2 2\theta_{13} = 0.1$. Contributions come from the unoscillated intrinsic contamination of the beam ν_e and $\bar{\nu}_e$ CC events, the electrons (positrons) from $\nu_\mu \to \nu_e$ ($\bar{\nu}_\mu \to \bar{\nu}_e$) oscillations, and from $\nu_\mu \to \nu_\tau$ oscillations followed by the decay of the tau into electron. The oscillations effects are clearly visible and we will use these distributions to build the χ^2 function.

4.5   Results from CNGS appearance data only

The χ^2_{CNGS-e} is computed as

$$\chi^2_{CNGS-e} = \sum_{E^{vis}, P_T^{miss}, P_T^e} \left(\frac{N - N^{ref}}{\Delta N} \right)^2 \tag{4.4}$$

where the sum runs over every bin on the E^{vis}, P_T^{miss} and P_T^e distributions (100 bins per histogram). ΔN is the statistical error added in quadrature to the systematic error. The systematic errors are a 10% uncorrelated error on each bin and an uncorrelated 10% error in the τ electron spectrum (which also takes into account the error on the tau detection efficiency).

As evident from equations 4.2 and 4.3 valid for small values of L/E, the $\nu_\mu \to \nu_\tau$ oscillation probability is the product of terms involving θ_{13}, θ_{23} and Δm^2_{32}. Hence the angles and the Δm^2_{32} cannot be measured independently by electron appearance data only. This is illustrated in Figure 4.2, where the χ^2_{CNGS-e} contour is plotted for Δm^2_{32} vs $\sin^2 2\theta_{23}$, leaving $\sin^2 2\theta_{13}$ free. Electron appearance data is clearly insufficient to measure to a high level of accuracy both parameters and therefore additional independent observables that constrain either the mixing angle or Δm^2_{32} are needed to improve the result.

Figure 4.3 shows the one dimensional χ^2_{CNGS-e} behaviour for the three parameters independently. The one- and two- sigma levels are shown by horizontal lines. When computing the χ^2 for one parameter, the other two are left free. The band that was
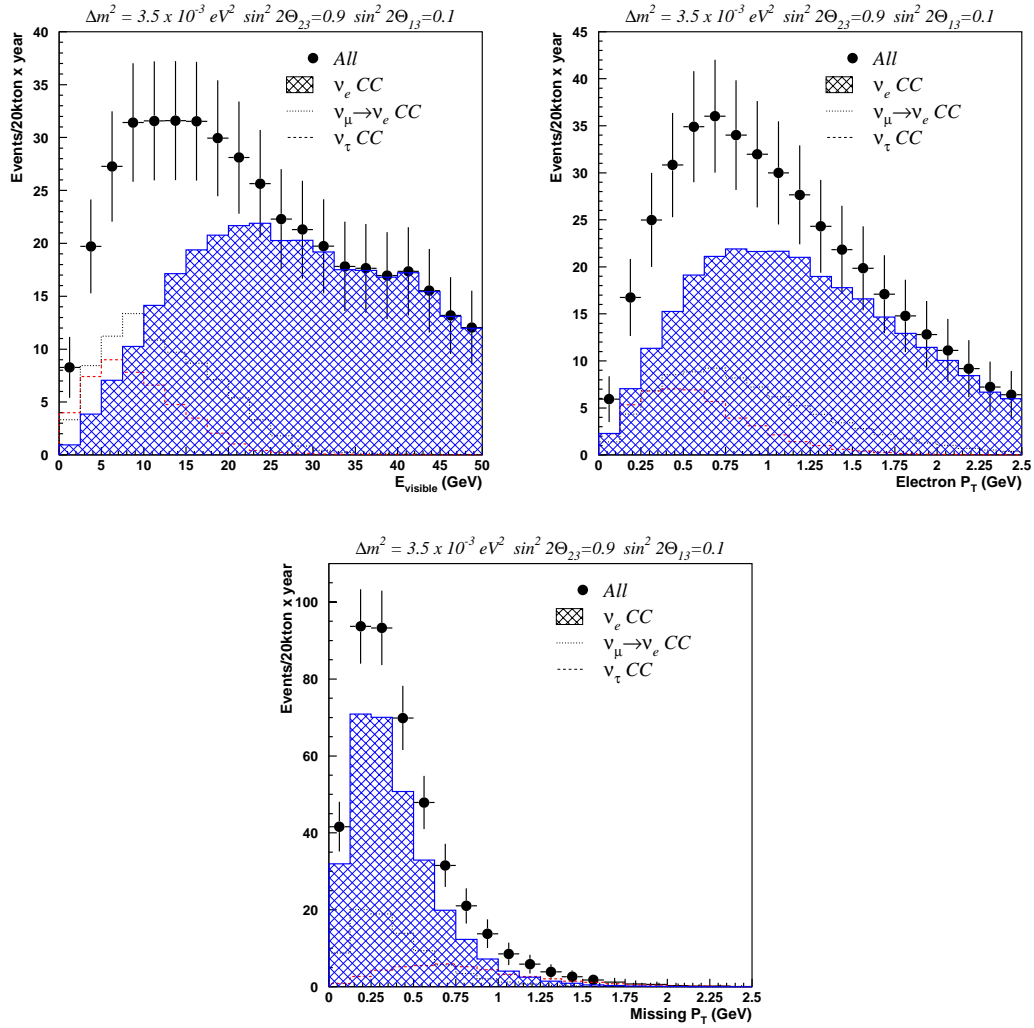
Figure 4.1: e-appearance beam data: Distribution of the total visible energy E_{vis}, the transverse momentum of the electron P_T^e and the total missing transverse momentum P_T^{miss} under the reference oscillation parameters.

visible in the 2 dimension contour of Figure 4.2 translates into a poor determination of the mass and the mixing angle $\sin^2 2\theta_{23}$.

4.5.1 Disappearance signature

Muon neutrino disappearance measurements provide additional handles to constrain the value of Δm_{32}^2 by measuring the location of the maximum disappearance *dip* in the visible energy spectrum. Since we do not rely on a near station measurement to predict the unoscillated energy spectrum, we conservatively assume a large systematic uncertainty in the knowledge of the beam. This error amounts to a 30% uncorrelated error on each bin of the histogram distribution. In addition, we do not consider events at energies below 3 GeV.

We certainly believe that these provide conservative estimates.

The upper plot of Figure 4.4 shows (as crosses) the visible energy spectrum of ν_μ CC events in case of no oscillations. Possible oscillated spectra are overlapped as histograms for the following three values of Δm_{32}^2: 1.5×10^{-3}, 3.5×10^{-3} and $6 \times 10^{-3}\text{eV}^2$. The lower plot in Figure 4.4 displays the ratio of the oscillated spectrum to the expected spectrum in case of no oscillations. The horizontal band corresponds to our 30% systematic error and the region below 3 GeV is also shaded since we do not consider these events.

Given the baseline between CERN and Gran Sasso laboratories, the disappearance effect is expected to be dramatic at low energies, especially for the lower Δm_{32}^2 values of the allowed atmospheric region.

It is clear from the figure that an improved knowledge of the beam, in particular in the region below 3 GeV will provide a much better information on the disappearance signal. We are confident that indeed we will be able to obtain a better systematic knowledge of the beam and use the events at very low energy.

Meanwhile, we conservatively do not envisage the possibility to use the events inside the shaded area of Figure 4.4. The point is that a precise knowledge of the beam is not a crucial issue since the combination of the appearance and atmospheric data yields already a precise determination of the oscillation parameters, as it will be shown later.

4.5.2 Results from CNGS disappearance data only

The $\chi^2_{CNGS-\mu}$ is computed as

$$\chi^2_{CNGS-\mu} = \sum_{E^{vis}} \left(\frac{N - N^{ref}}{\Delta N} \right)^2 \tag{4.5}$$

where the sum runs over every bin on the E^{vis} distributions (100 bins). ΔN is the statistical error added in quadrature to the systematic error. The considered systematic errors amount up to a 30% uncorrelated error on each bin.

Figure 4.5 shows the $\chi^2_{CNGS-\mu}$ behaviour for two reference Δm_{32}^2 values: 3.5×10^{-3} (dashed line) and $6 \times 10^{-3}\text{eV}^2$ (solid line). Here for each value of Δm_{32}^2 ($\sin^2 2\theta_{23}$) we minimize $\chi^2_{CNGS-\mu}$ leaving the other two parameters free. For the lower Δm_{32}^2 value, the maximum disappearance *dip* in the visible energy spectrum lies below the considered
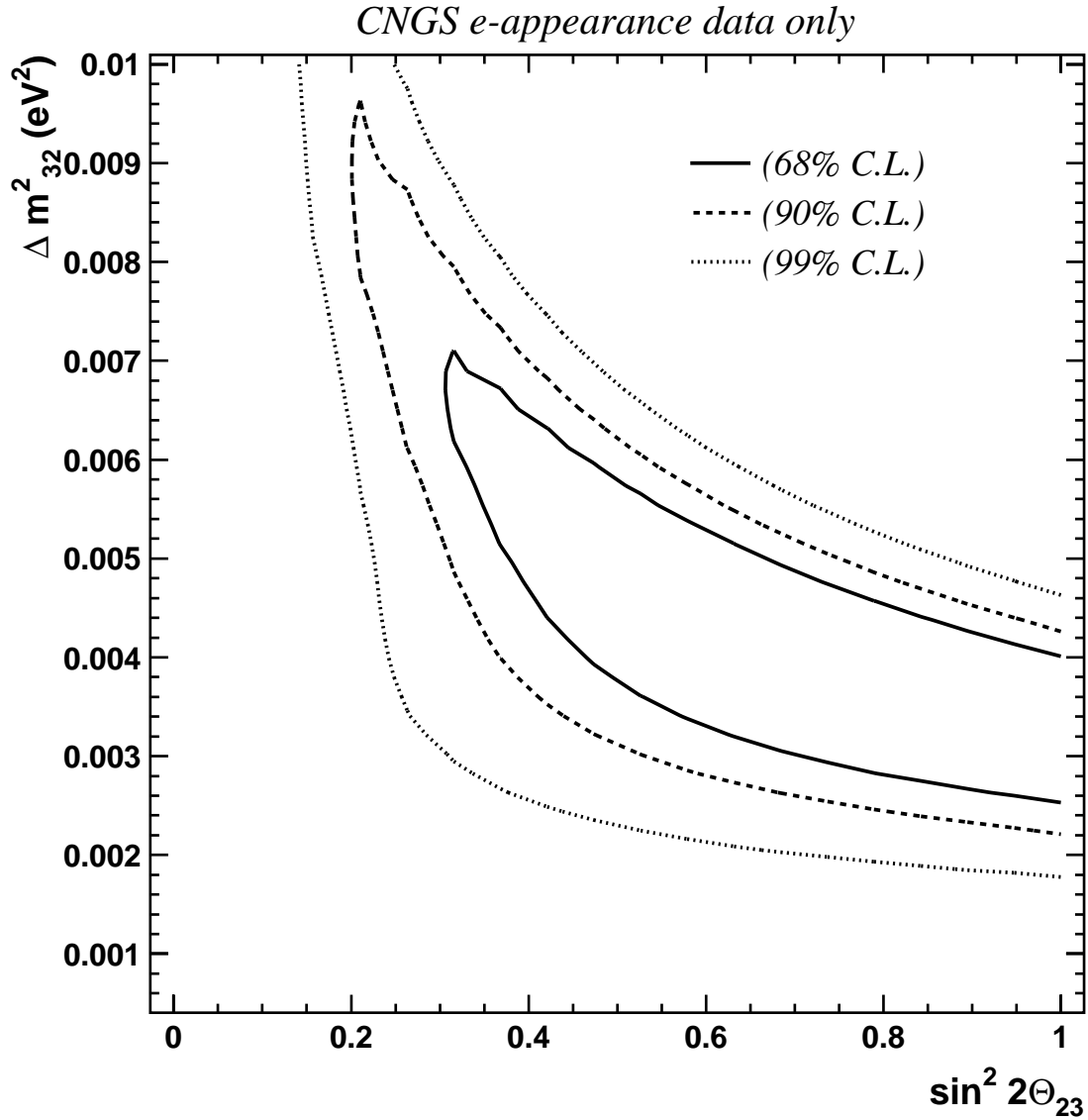
Figure 4.2: Determination of the parameters Δm_{32}^2 versus $\sin^2 2\theta_{23}$ using the CNGS electron appearance data only. The χ^2 value of the fit is plotted as a function of the two parameters. When computing the χ^2, the $\sin^2 2\theta_{13}$ parameter is left free. The 68%, 90% and 99% corresponds to respectively $\chi^2 + 2.4$, $+4.6$, and $+9.2$ regions.
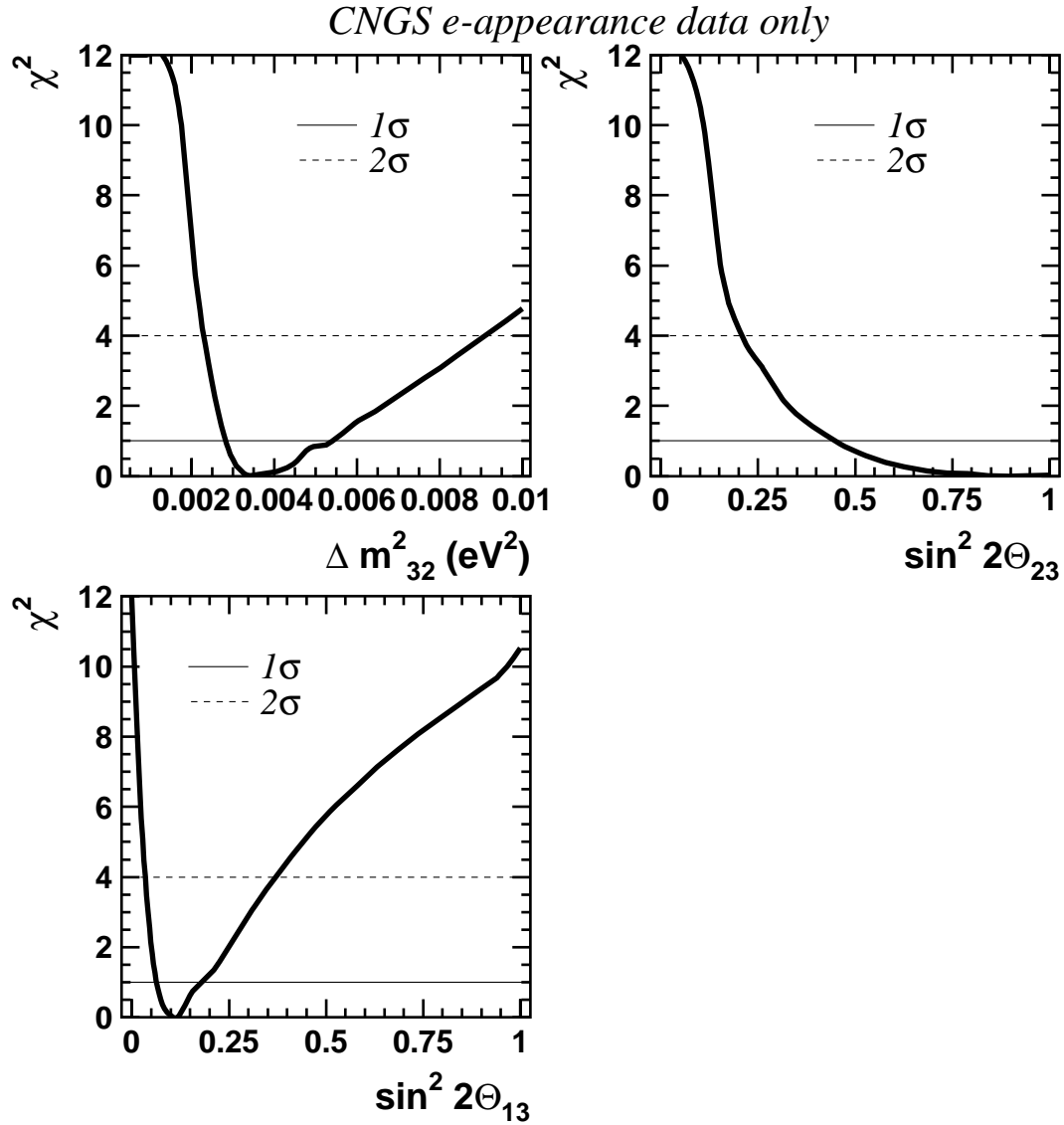
Figure 4.3: Determination of the parameters Δm_{32}^2, $\sin^2 2\theta_{23}$ and $\sin^2 2\theta_{13}$ using the CNGS electron appearance data only. For each plot, the χ^2 value of the fit is plotted as a function of one parameter. When computing the χ^2 for one parameter, the other two are left free. The one- and two- sigma levels are shown by horizontal lines.
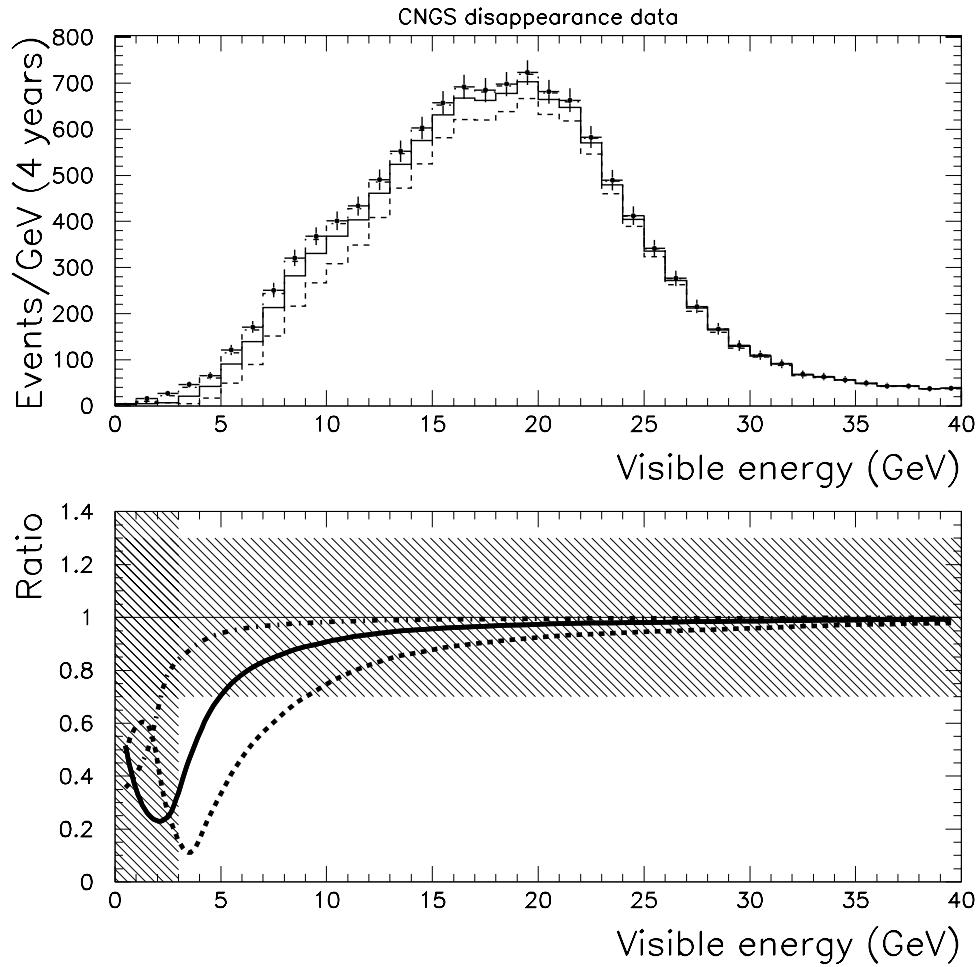
Figure 4.4: Upper plot: visible energy distribution of the ν_μ CC sample. Lower plot: ratio of the observed distribution in case of $\nu_\mu \to \nu_X$ oscillations to the expected without oscillations. The following three values of Δm^2_{32} have been chosen: 1.5×10^{-3}, 3.5×10^{-3} and $6 \times 10^{-3} \mathrm{eV}^2$.

energy threshold. The uncertainty in the location of the *dip* translates into a lack of prediction power for the oscillation parameters. Even at 1σ level the information provided by the CNGS disappearance data is certainly poor.

On the other hand, for $\Delta m_{32}^2 = 6 \times 10^{-3} \mathrm{eV}^2$ the *dip* lies at about 4GeV and therefore can be located with higher precision. The observation of the oscillatory behaviour translates into a better determination of Δm_{32}^2. Moreover the depth of the dip, related to the amplitude of the oscillation, is more precisely determined, thus a better determination of the mixing angle is expected. Figure 4.5 shows how the determination of the parameters improves for larger values of Δm_{32}^2 (when a more precise measurement of the maximum disappearance *dip* in the visible energy spectrum is achieved). Figure 4.6 shows, for the larger reference value of Δm_{32}^2, the contour for Δm_{32}^2 vs $\sin^2 2\theta_{23}$ obtained when $\sin^2 2\theta_{13}$ is left free.

4.6   The atmospheric data

Measurements of atmospheric neutrinos are described in detail inside the proposal. Here we recall *ICANOE* will provide in addition to comfortable statistics, an observation of atmospheric neutrinos with a much improved quality compared to that currently obtained in SuperKamiokande. This will be accompanied by an improvement of the precision of theoretical prediction both for the fluxes and for neutrino interactions. We have considered the following three methods:

- ν_μ **disappearance**: detection of the oscillation pattern in the L/E distribution, where L is the neutrino pathlength and E its energy;

- ν_τ **appearance** : comparison of the NC/CC with expectation;

- **direct** ν_τ **appearance** : comparison of upward and downward rates of "tau-like" events.

together with the well established ones:

- **the double ratio,** $(\nu_\mu/\nu_e)_{obs}/(\nu_\mu/\nu_e)_{MC}$;

- **up/down asymmetry**;

- **the zenith angle distributions for electrons and muons**;

Muon measurement is crucial to most atmospheric neutrino analyses. In *ICANOE*, we achieve the required performances using the multiple scattering measurement. The high granularity imaging allows in addition the identification and measurement of electrons and individual hadrons in the event.

The rates for the different neutrino processes for the different exposures are quoted in Table 4.2.

The absolute predictions of the atmospheric neutrino rates have however an uncertainty of $\pm 20\%$, originating mostly from the uncertainties in the absolute intensity of the primary cosmic ray flux, in the nuclear interaction models and last but not least
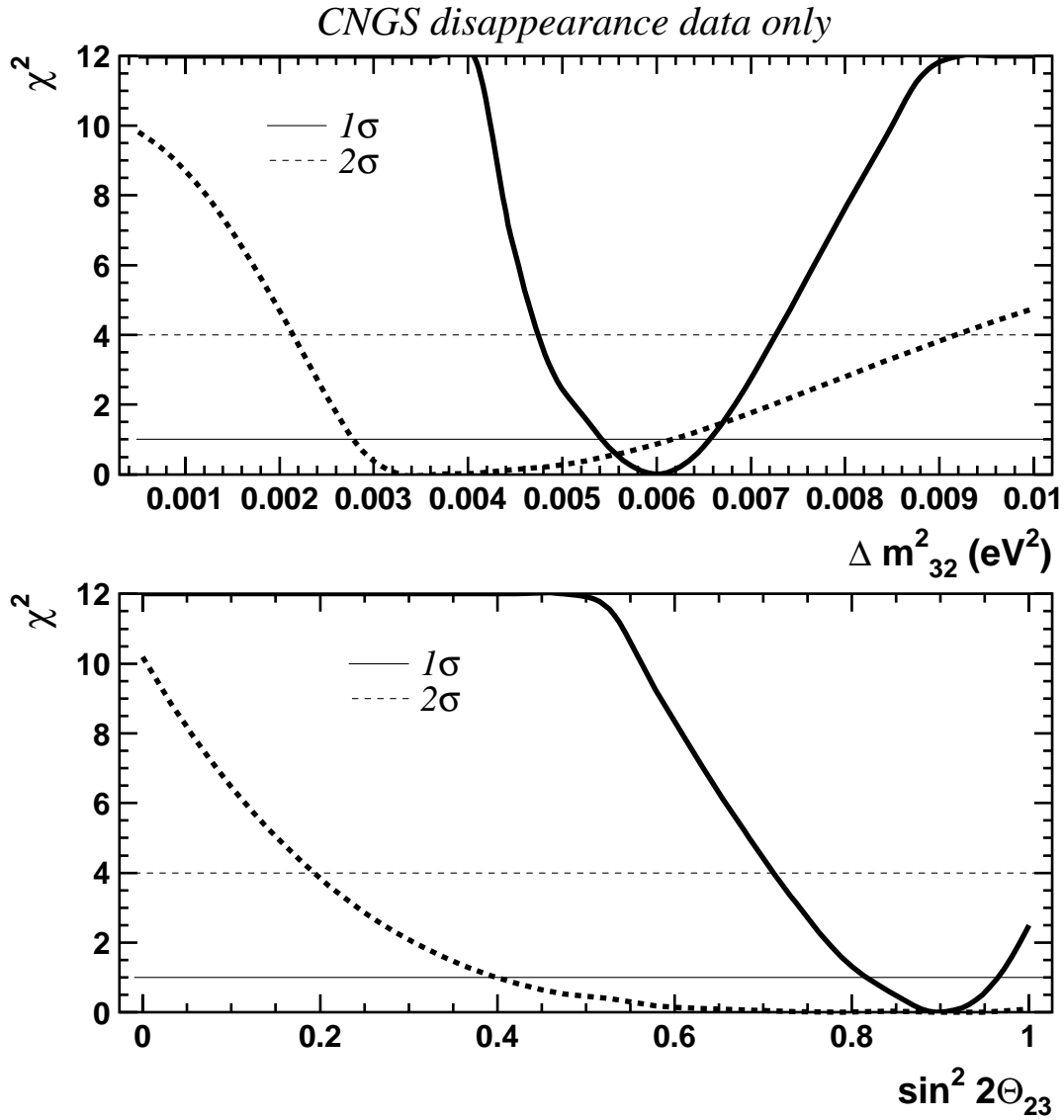
Figure 4.5: Determination of the parameters Δm^2_{32}, $\sin^2 2\theta_{23}$ and $\sin^2 2\theta_{13}$ using the CNGS disappearance data only. For each plot, the χ^2 value of the fit is plotted as a function of one parameter. When computing the χ^2 for one parameter, the other two are left free. The one- and two- sigma levels are shown by horizontal lines.
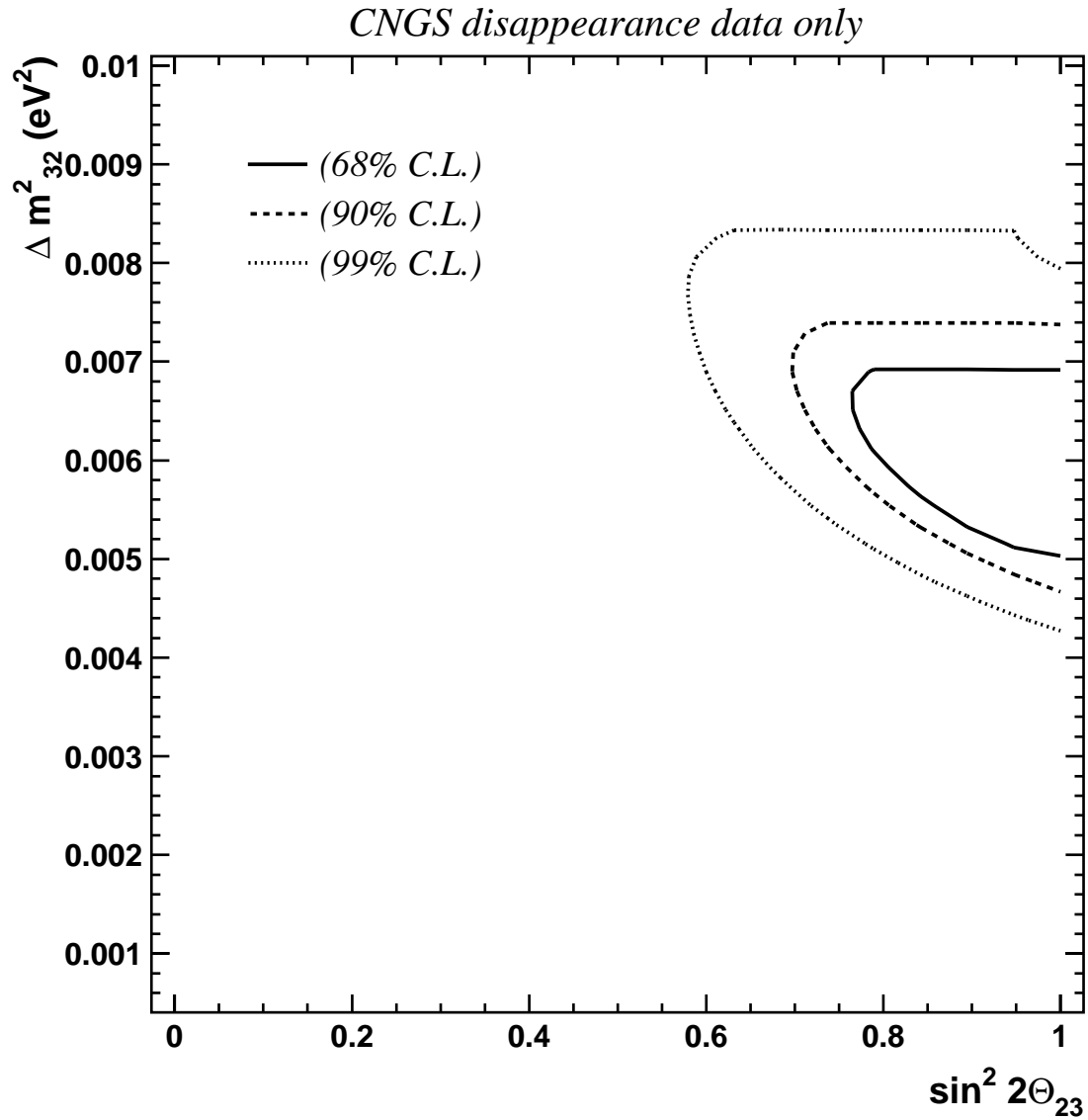
Figure 4.6: Determination of the parameters Δm_{32}^2 vs $\sin^2 2\theta_{23}$ using the CNGS disappearance data only. When computing the χ^2, the $\sin^2 2\theta_{13}$ parameter is left free. The 68%, 90% and 99% corresponds to respectively $\chi^2 + 2.4$, $+4.6$, and $+9.2$ regions.

Process	Exposure		
	5 kton× year	20 kton×year	50 kton× year
ν_μ CC	535	2140	5350
$\bar{\nu}_\mu$ CC	135	545	1350
ν_e CC	300	1200	3000
$\bar{\nu}_e$ CC	59	235	585
ν NC	325	1300	3250
$\bar{\nu}$ NC	150	590	1500

Table 4.2: Unoscillated atmospheric neutrino events on Argon for exposures of 5, 20 and 50 kton×years.

in the ν-nucleus cross sections in the energy range of interest. On the other hand, the flavour ratio of the atmospheric neutrino flux, $(\nu_\mu + \bar{\nu}_\mu)/(\nu_e + \bar{\nu}_e)$, is believed to be known to an accuracy of better than 5% in a broad energy range from 0.1 GeV to higher than 10 GeV since most of the experimental and theoretical uncertainties cancel out, especially the uncertainty in the absolute flux. The measurements have been traditionally reported as $R \equiv (\mu/e)_{data}/(\mu/e)_{MC}$, where μ and e are the number of muon-like (μ-like) and electron-like (e-like) events observed in the detector for both data and Monte Carlo (MC) simulation. However, the double ratio, since integrated over neutrino energies and pathlengths, is unable to provide precise constraints on Δm_{32}^2.

Despite the larger systematic uncertainties associated to the electron and muon neutrino absolute fluxes, we fit absolute zenith angle distributions of electron and muons separately, in four visible energy bins.

In Figure 4.7 we show the zenith angle distributions for different visible energy ranges for electrons and muons samples separately. The solid line corresponds to the no oscillation case, while dots corresponds to neutrino oscillations occurring with $\Delta m_{32}^2 = 3.5$ eV^2 $\sin^2 2\theta_{23} = 0.9$ and $\sin^2 2\theta_{13} = 0.1$. The zenith angle has been reconstructed taking into account all the measured final state particles.

4.6.1 Results from atmospheric data only

The χ^2 for the atmospheric neutrinos is given by:

$$\chi_{atm}^2 = \sum_{\cos\theta, \, E^{vis}} \left(\frac{N - N^{ref}}{\Delta N} \right)^2 \tag{4.6}$$

where the sum is over ten bins equally spaced in $\cos\theta$ and four bins in visible energy for both electron and muon events. The systematic error is taken to be a 20% uncorrelated error in each bin.

Figure 4.8 shows the χ^2 behaviour for each parameter independently leaving the other two free. The capability to unambiguously discriminate between electron and muon events allows to constrain the mixing angles in a precise way. Since a large muon deficit is observed, this forces the mixing angles to be close to maximal. However, since electrons
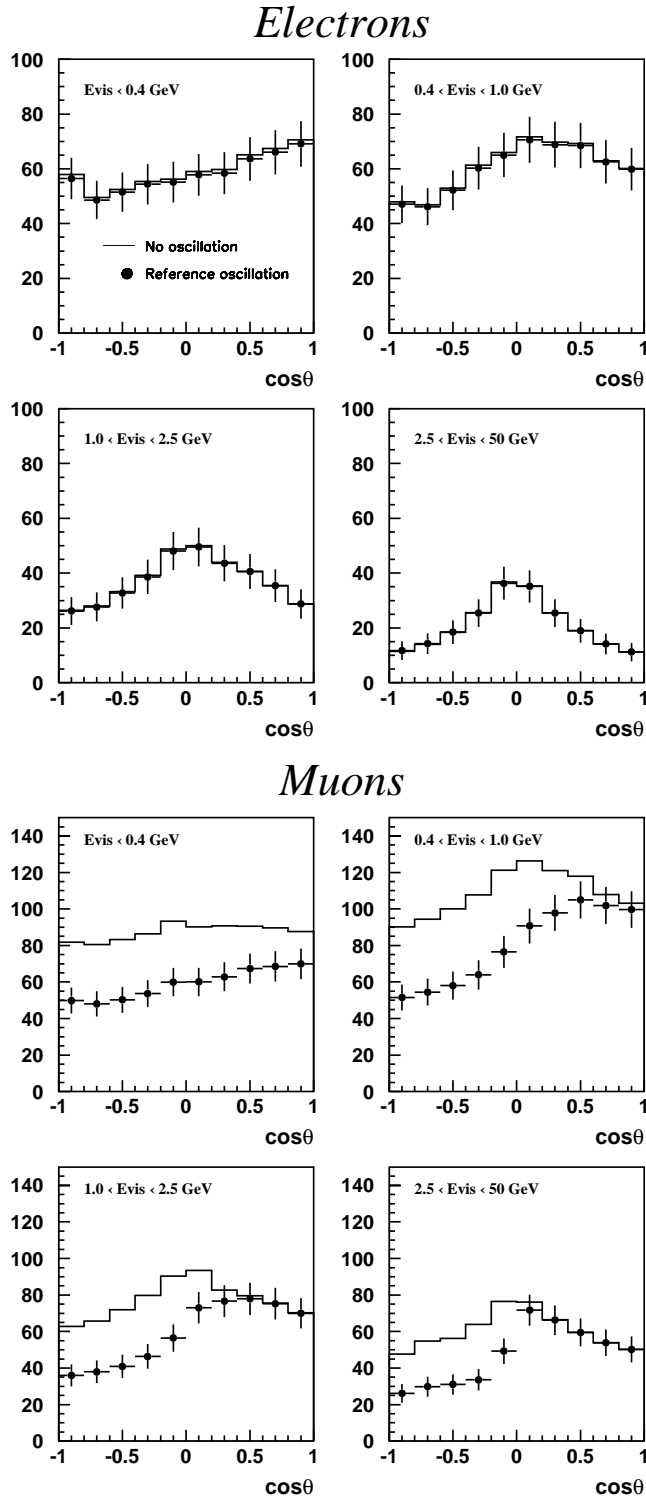
Electrons

Muons

Figure 4.7: Zenith angle distributions for electrons (top plots) and muons (bottom plots) in several visible energy bins. Solid lines correspond to the no oscillation case. Dots refer to the oscillation case with parameters: $\Delta m^2 = 3.5 \times 10^3$, $\sin^2 2\theta_{23} = 0.9$ and $\sin^2 2\theta_{13} = 0.1$.

Systematic errors	
CNGS muon data:	
muon spectrum uncorrelated bin-to-bin	±30%
CNGS electron data:	
electron spectrum uncorrelated bin-to-bin	±10%
tau spectrum uncorrelated bin-to-bin	±10%
atmospheric data:	
Zenith angle distributions:	±20%

Table 4.3: List of systematic errors, unless otherwise noted, assumed in the determination of the oscillation parameters.

do not disappear, θ_{13} is constrained to small values and therefore forces θ_{23} to its correct large value.

4.7 Combined χ^2 fit

We combine the information coming from CNGS appearance and disappearance data and atmospheric neutrinos:

$$\chi^2 = \chi^2_{CNGS-e} + \chi^2_{CNGS-\mu} + \chi^2_{atm} \tag{4.7}$$

Table 4.3 summarizes the systematic errors assumed for each data set in the combined fit.

The effect on the determination of the oscillation parameters brought about by the combination of the different observables measurable in *ICANOE* is clearly visible in Figure 4.9 where the CNGS electron appearance data is fitted along with the atmospheric data.

The atmospheric data alone imposed a constraint on $\sin^2 2\theta_{23}$ which, when combined with the CNGS electron appearance data drastically improves the precision in the measurement of Δm^2_{32}, $\sin^2 2\theta_{23}$. Moreover, the capability to discriminate ν_e's from ν_τ's allows an accurate determination of the mixing angle θ_{13} as well.

The measurement of the parameters is slightly improved when the CNGS disappearance data is included. The effect can be seen in Figure 4.10. A precise determination of the oscillation parameters does not crucially depend on a precise knowledge of ν_μ component of the beam, since the main constraints are provided by the atmospheric and the appearance data.

We also show contours for pairs of parameters. The results can be observed in Figure 4.11 (Δm^2_{32} versus $\sin^2 2\theta_{23}$) and Figure 4.12 ($\sin^2 2\theta_{23}$ versus $\sin^2 2\theta_{13}$) where the allowed parameter regions at the 68%, 90% and 99% C.L. are drawn. We observe that by combining all the available data sets, the region of allowed values is reduced to a small closed region of the parameter space.
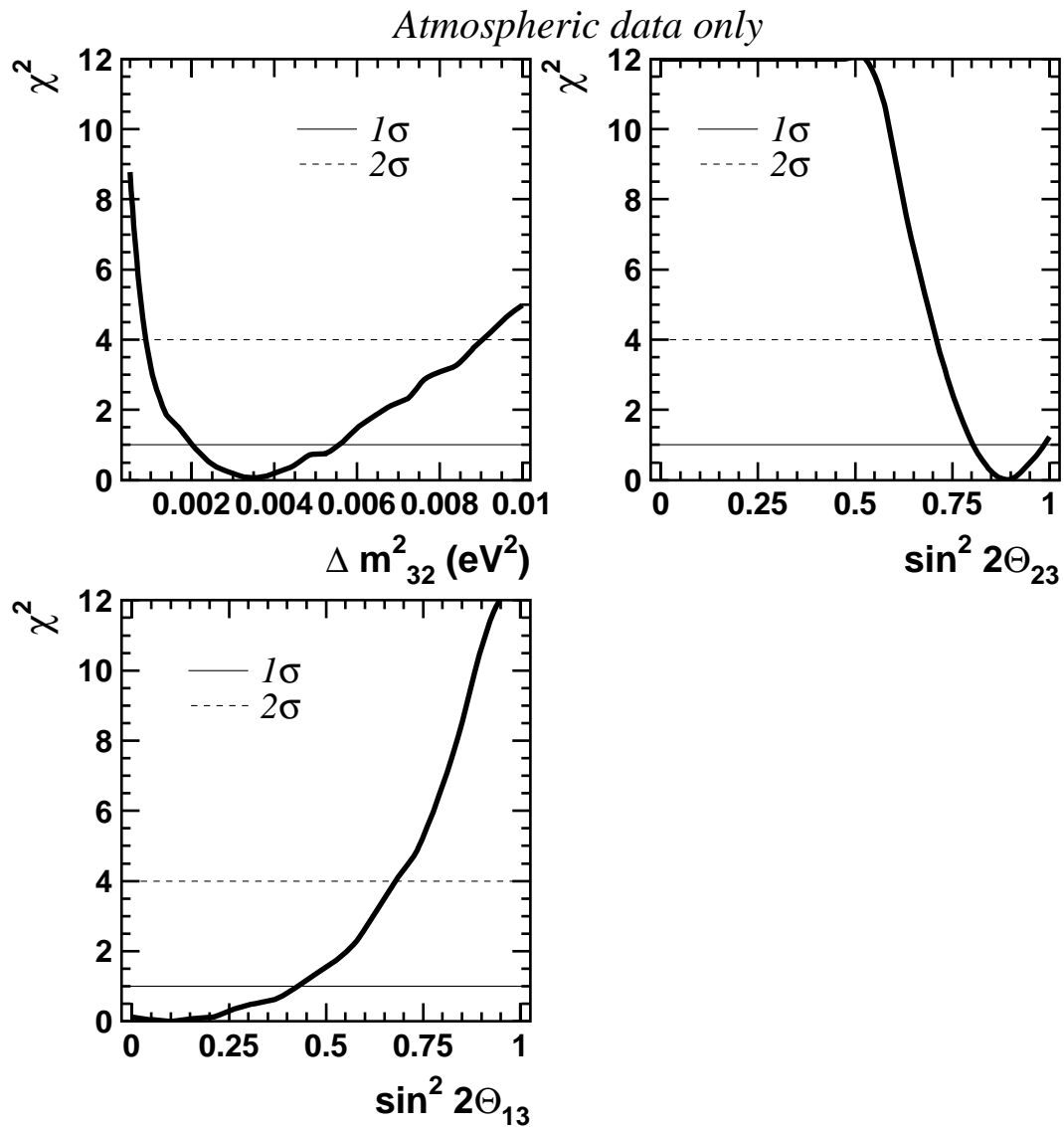
Figure 4.8: Determination of the parameters Δm_{32}^2, $\sin^2 2\theta_{23}$ and $\sin^2 2\theta_{13}$ using the atmospheric data only. For each plot, the χ^2 value of the fit is plotted as a function of one parameter. When computing the χ^2 for one parameter, the other two are left free. The one- and two- sigma levels are shown by horizontal lines.
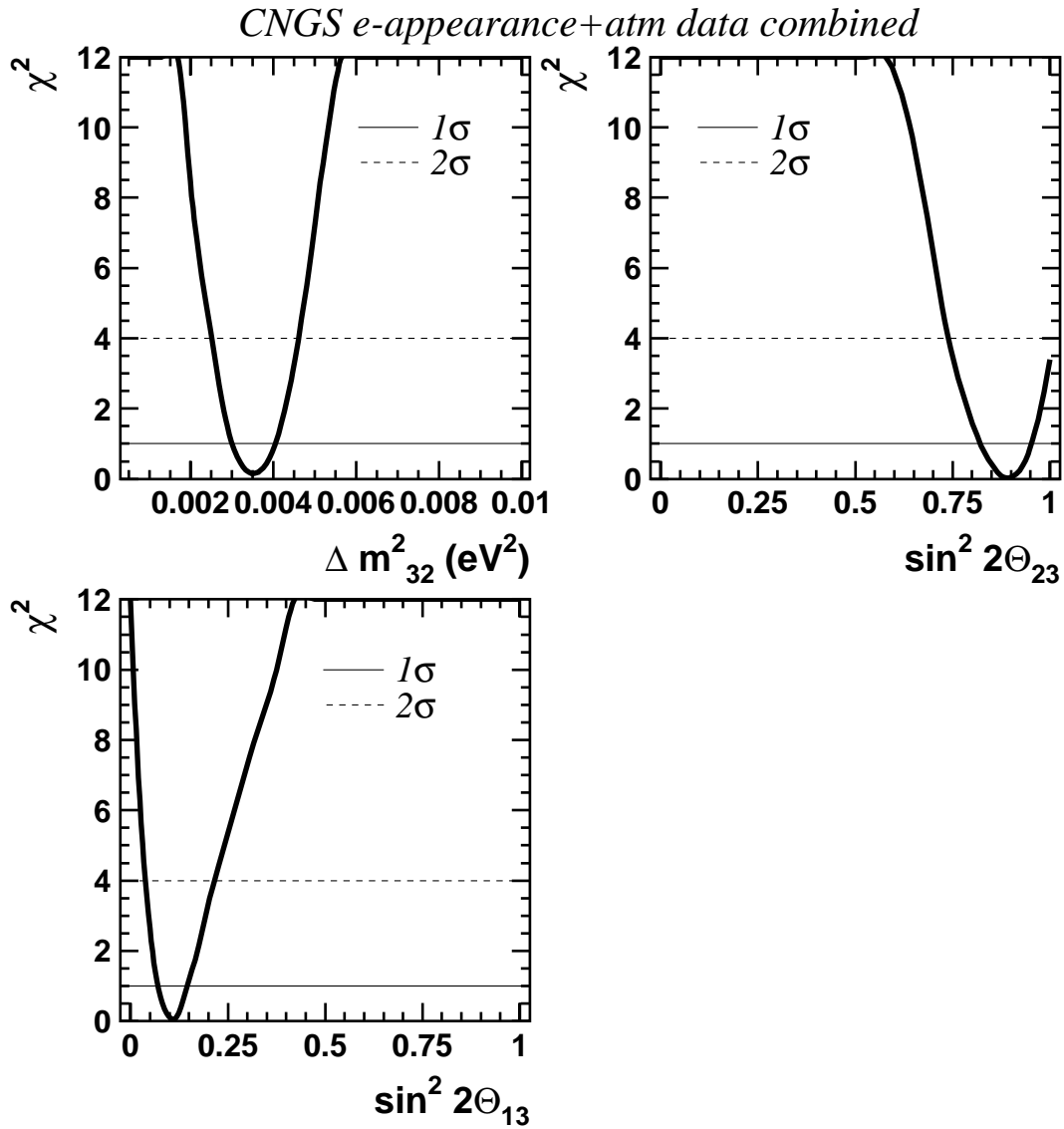
Figure 4.9: Determination of the parameters Δm^2_{32}, $\sin^2 2\theta_{23}$ and $\sin^2 2\theta_{13}$ using the CNGS electron appearance data and the atmospheric data. For each plot, the χ^2 value of the fit is plotted as a function of one parameter. When computing the χ^2 for one parameter, the other two are left free. The one- and two- sigma levels are shown by horizontal lines.
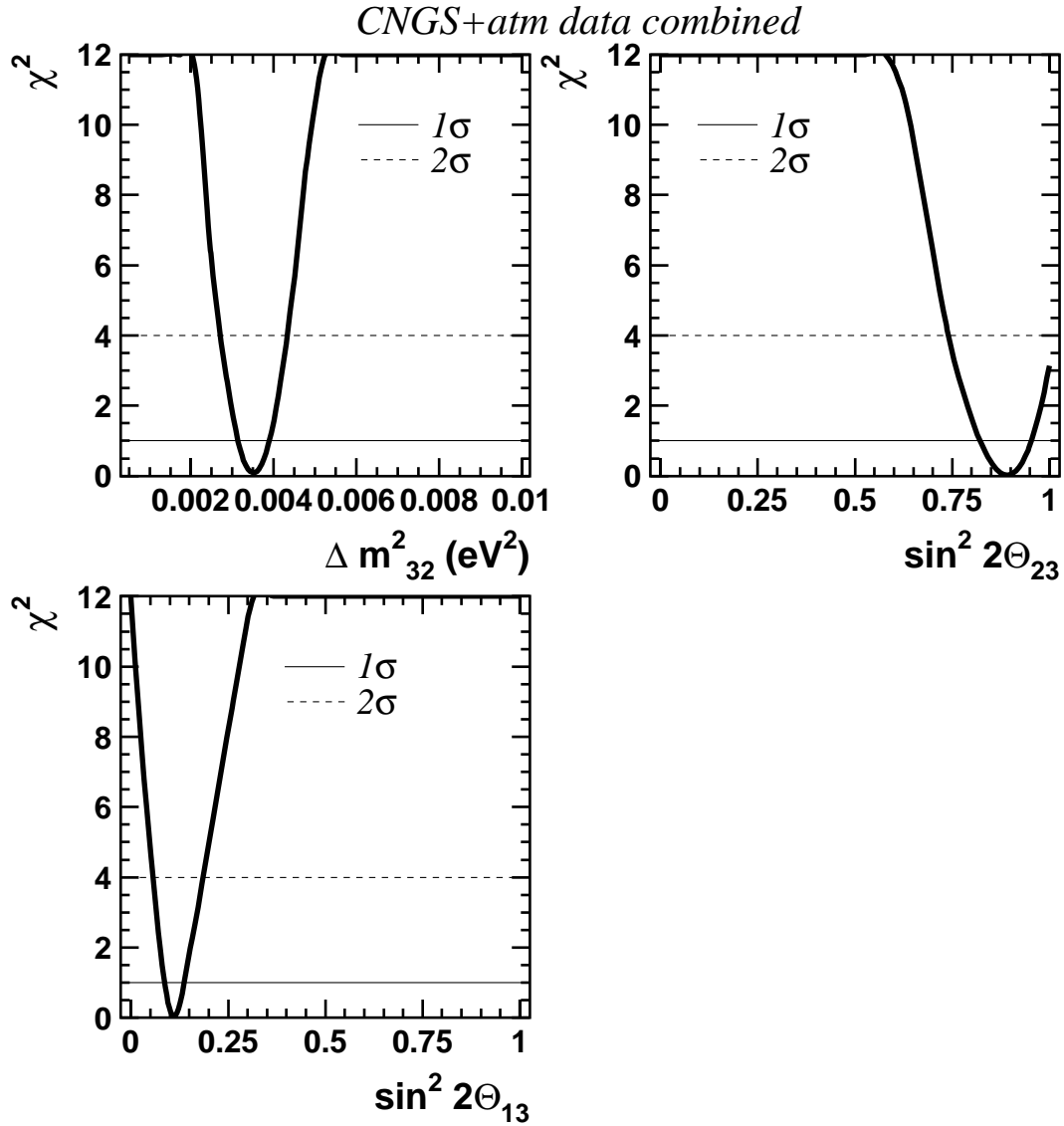
Figure 4.10: Determination of the parameters Δm^2_{32}, $\sin^2 2\theta_{23}$ and $\sin^2 2\theta_{13}$ using the CNGS electron appearance and disappearance data combined with atmospheric data. For each plot, the χ^2 value of the fit is plotted as a function of one parameter. When computing the χ^2 for one parameter, the other two are left free. The one- and two- sigma levels are shown by horizontal lines.
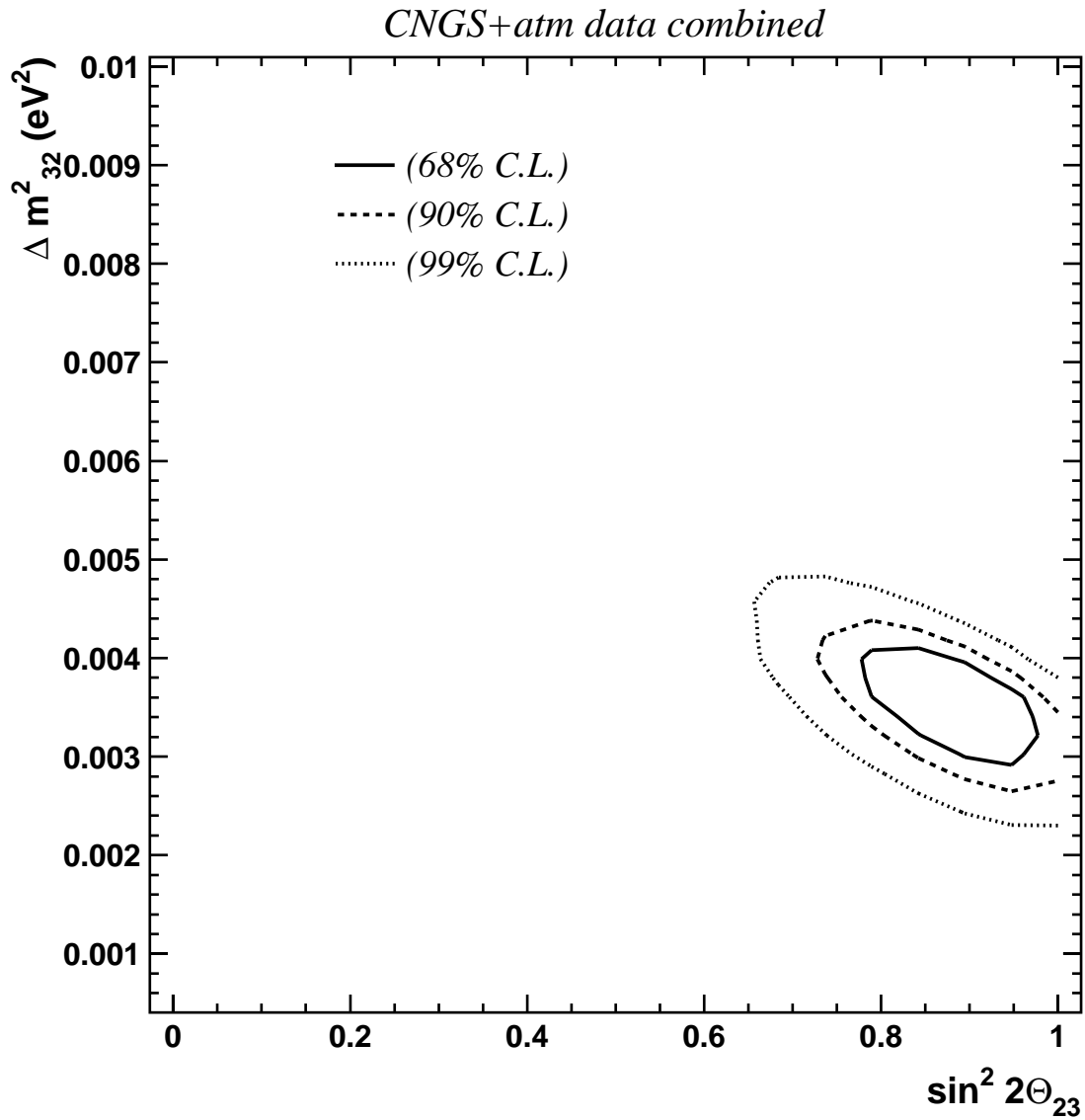
Figure 4.11: Determination of the parameters Δm^2_{32}, $\sin^2 2\theta_{23}$ using the CNGS electron appearance and disappearance data combined with atmospheric data. For each plot, the χ^2 value of the fit is plotted as a function of two parameters. When computing the χ^2 for two parameters, the third one is left free. The 68%, 90% and 99% corresponds to respectively $\chi^2 + 2.4$, $+4.6$, and $+9.2$ regions.
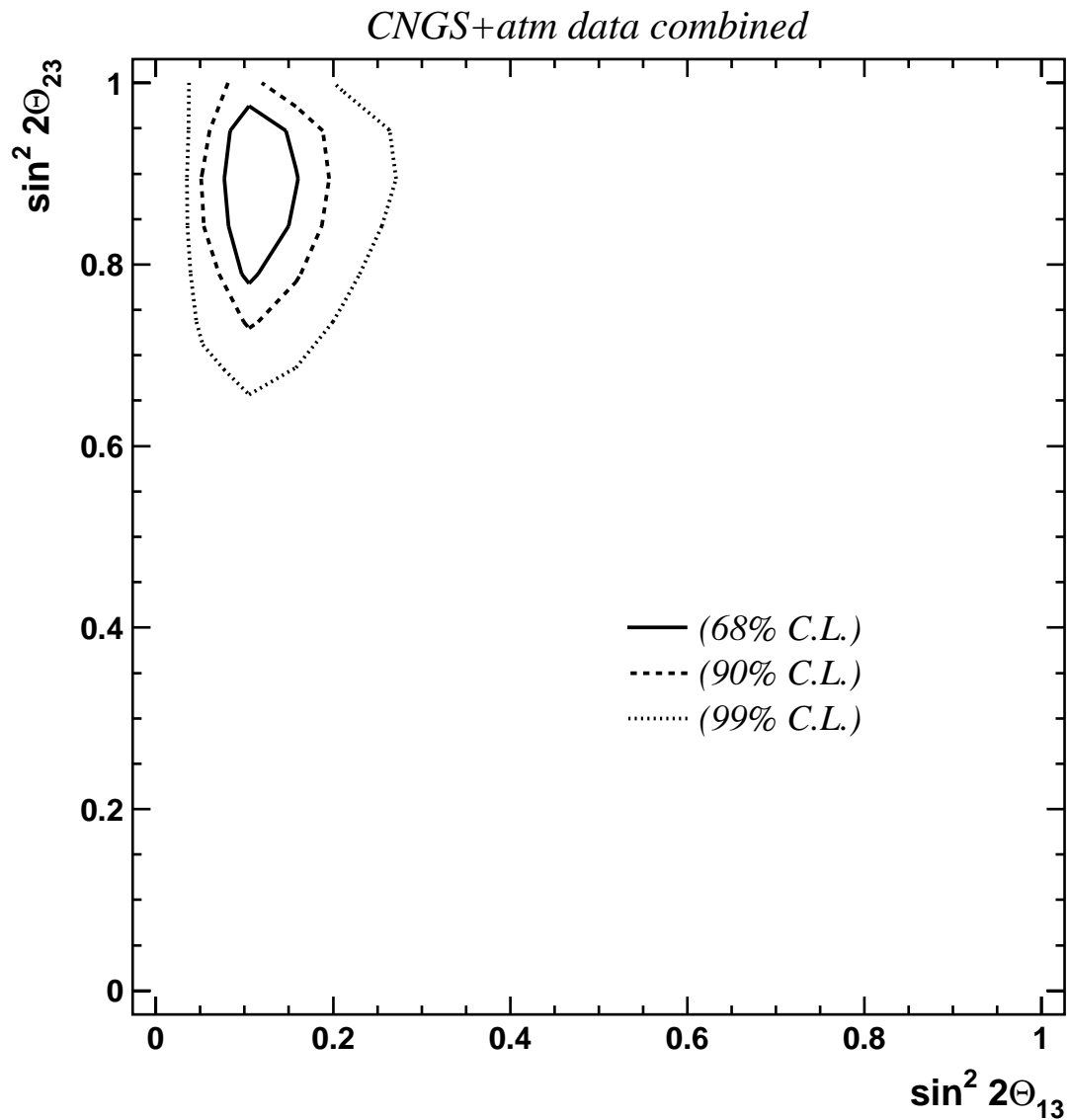
Figure 4.12: Determination of the parameters $\sin^2 2\theta_{23}$ and $\sin^2 2\theta_{13}$ using the CNGS electron appearance and disappearance data combined with atmospheric data. For each plot, the χ^2 value of the fit is plotted as a function of two parameters. When computing the χ^2 for two parameters, the third one is left free. The 68%, 90% and 99% corresponds to respectively $\chi^2 + 2.4$, $+4.6$, and $+9.2$ regions.

To demonstrate how well we can constrain the oscillation parameters when CNGS electron appearance and atmospheric data are combined, we compare in Figure 4.13 our estimation of the parameters with that provided by the Kamiokande and SuperKamiokande collaborations (dashed lines represent allowed values at 90% C.L.). Our estimation of the parameters take as reference oscillation values: $\Delta m_{32}^2 = 3.5\text{eV}^2$, $\sin^2 2\theta_{23} = 1$, $\sin^2 2\theta_{13} = 0$. We show (solid lines) the allowed parameters contours at 68%, 90% and 99% corresponding to $\chi_{min}^2 + 2.6$, $+5.0$, and $+9.6$ regions (these values take into account the fact that our parameters should lie inside a bounded physical region). The combination of beam appearance and atmospheric data results in a very precise determination of Δm_{32}^2.

4.8 Summary

We have considered the most general 3-neutrino mixing scenario determined by three parameters: Δm_{32}^2, $\sin^2 2\theta_{13}$ and $\sin^2 2\theta_{23}$. We show that *ICANOE* provide an excellent determination of these parameters by combining the appearance and disappearance signatures from the CNGS beam together with the atmospheric measurements. The fits we have performed already include large but conservative systematic errors which clearly demonstrates that our method realistically provides a precise determination of the oscillation parameters.

For example, given the reference parameters considered, and for a total exposure of 20 kton×year for beam neutrinos and 25 kton×year for atmospheric neutrinos, *ICANOE* would measure the parameters governing the oscillation with the following precisions:

$$
\begin{aligned}
\Delta m_{32}^2 &= (3.5 \pm 0.4) \times 10^{-3} \text{ eV}^2 \\
\sin^2 2\theta_{23} &= 0.90 \pm 0.12 \\
\sin^2 2\theta_{13} &= 0.10 \pm 0.04
\end{aligned}
\tag{4.8}
$$

4.9 Test of the LMA solution

The liquid target of *ICANOE* is particularly well fitted to study low energy electrons. This is exemplified in the direct observation of solar ^8B neutrinos with an electron threshold at about 5 MeV. Therefore, as already mentioned in the ICANOE proposal, atmospheric neutrinos will clearly be studied down to thresholds.

In particular, we foresee to study well the atmospheric neutrino electron spectrum below 1 GeV and down to 25 MeV. This range can, since coupled to a long baseline for upward going neutrinos, test the region of $E/L \approx 10^{-5} - 10^{-4} \text{ eV}^2$.

This means that the mass difference relevant to the MSW solution of the solar neutrino deficit can be studied with low energy atmospheric neutrinos crossing the Earth. In this case, we expect to observe a $\nu_e \leftrightarrow \nu_\mu$ oscillations with a $\Delta m^2 \approx 10^{-5} - 10^{-4} \text{ eV}^2$. Since the flux of ν_μ's is higher than that of ν_e's, an excess of neutrino electron events should be observed.
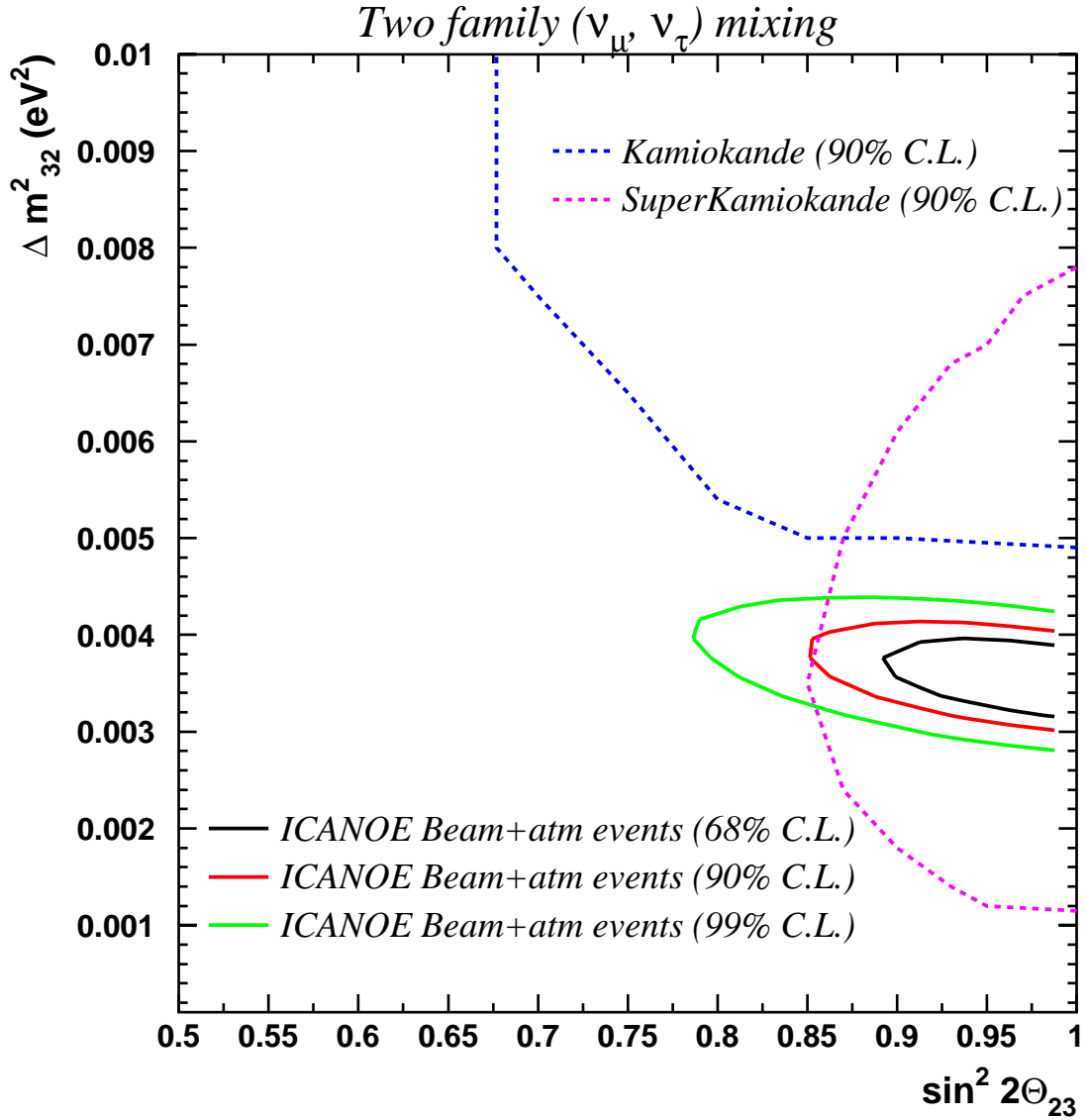
Figure 4.13: Determination of the parameters Δm_{32}^2, $\sin^2 2\theta_{23}$ using the CNGS electron appearance data and the atmospheric data assuming two-neutrino $\nu_\mu \rightarrow \nu_\tau$ maximal mixing $(\sin^2 2\theta_{23} = 1, \sin^2 2\theta_{13} = 0)$ in order to compare to SuperKamiokande and Kamiokande results (dashed lines correspond to a 90% C.L.). The 68%, 90% and 99% corresponds to respectively $\chi^2 + 2.6$, $+5.0$, and $+9.6$ regions.

$\nu_\mu \leftrightarrow \nu_e$ oscillations in matter			
Exposure ($kton \times year$)	ν_e CC no oscillations	ν_e CC oscillations	ν_e CC excess (%)
5	125	146	17 ± 10
20	500	585	17 ± 5
50	1249	1463	17 ± 3
Cuts: $E_{vis} < 1$ GeV, $\cos\theta_{zenith} < -0.2$			
Oscillation parameters: $\Delta m^2 = 9 \times 10^{-5}$ eV^2, $\sin^2 2\theta = 0.7$.			

Table 4.4: Atmospheric neutrino electron events in the low energy region for $\nu_\mu \leftrightarrow \nu_e$ oscillations with $\Delta m^2 = 9 \times 10^{-5}$ eV^2, $\sin^2 2\theta = 0.7$.

In addition, matter effects will change the oscillation probabilities since we are close to the MSW resonance region because of the neutrino energies involved[2].

We have studied these effects by considering a two-neutrino oscillation scenario relevant to the large mixing angle MSW solution (LMA) for the solar neutrino deficit: $\Delta m^2 = 9 \times 10^{-5}$ eV^2 and $\sin^2 2\theta = 0.7$. Note that this value is consistent with the day/night asymmetry observed in Superkamiokande.

Figure 4.14 shows the visible energy distribution of upward-going electron events below 1 GeV for an exposure of $20 kt \times year$. The shaded histogram corresponds to the expected spectrum without oscillations, while the dots indicate the spectrum with oscillations and its statistical error. A distortion of the visible energy spectrum is observable. Indeed, Figure 4.15(upper) shows the distribution of energy expected in case of oscillations normalized to the unoscillated spectrum.

The changes introduced by the matter effects can be seen by comparing Figure 4.15(upper) with the lower plot which neglects the presence of the Earth in the neutrino propagation. The spectral distortion with and without matter effects are different enough as to be able to effectively test for a given set of oscillation parameters the matter term in the neutrino propagation.

Tables 4.4 and 4.5 summarize these effects.

Work is in progress to include this information into the determination of the oscillation parameters described in the previous sections.

---

[2]Matter effects scale with neutrino energy times the matter density.
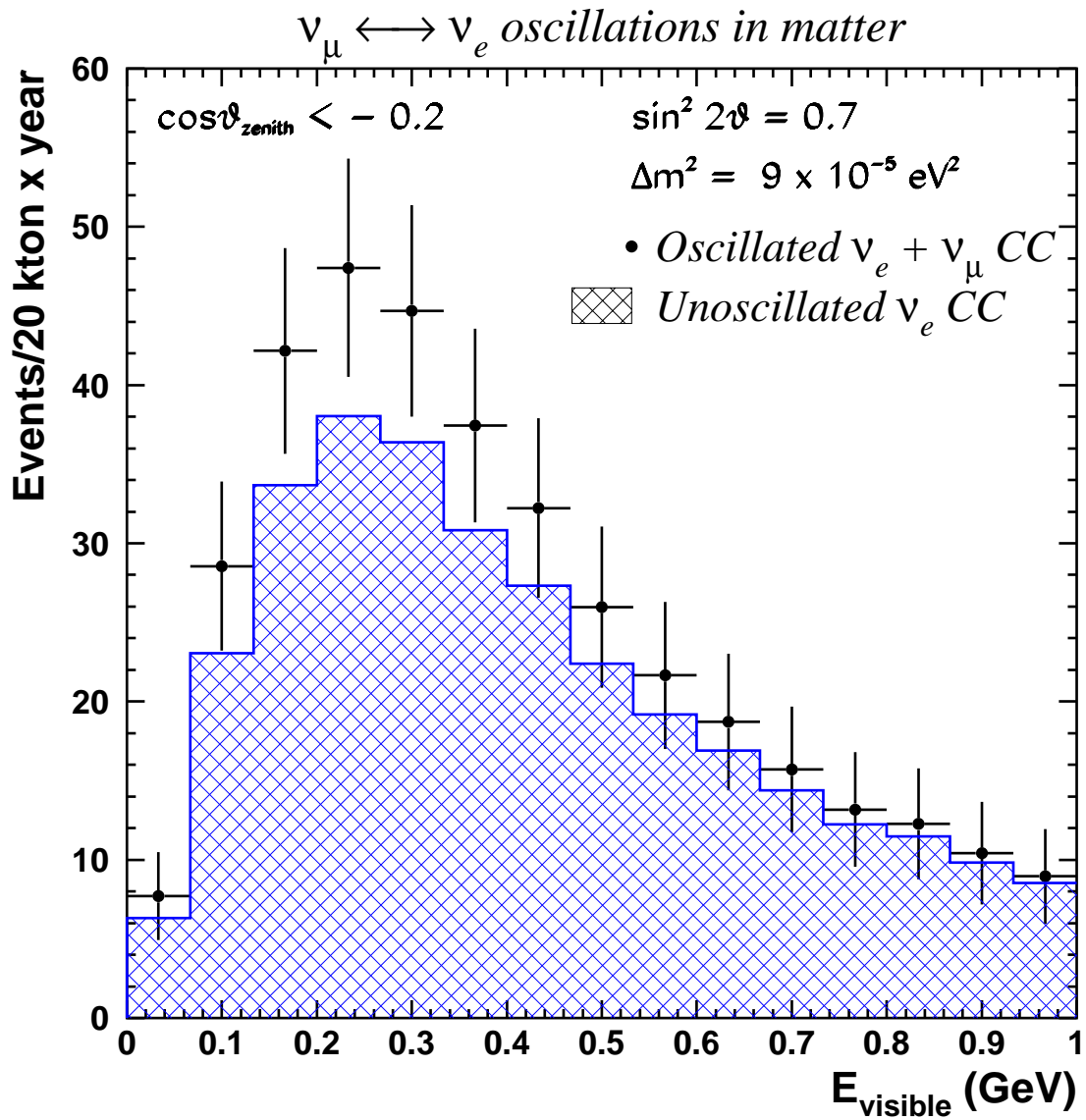
Figure 4.14:   Visible energy distributions compared for the no oscillation (dashed histogram) and oscillation (dots) case.
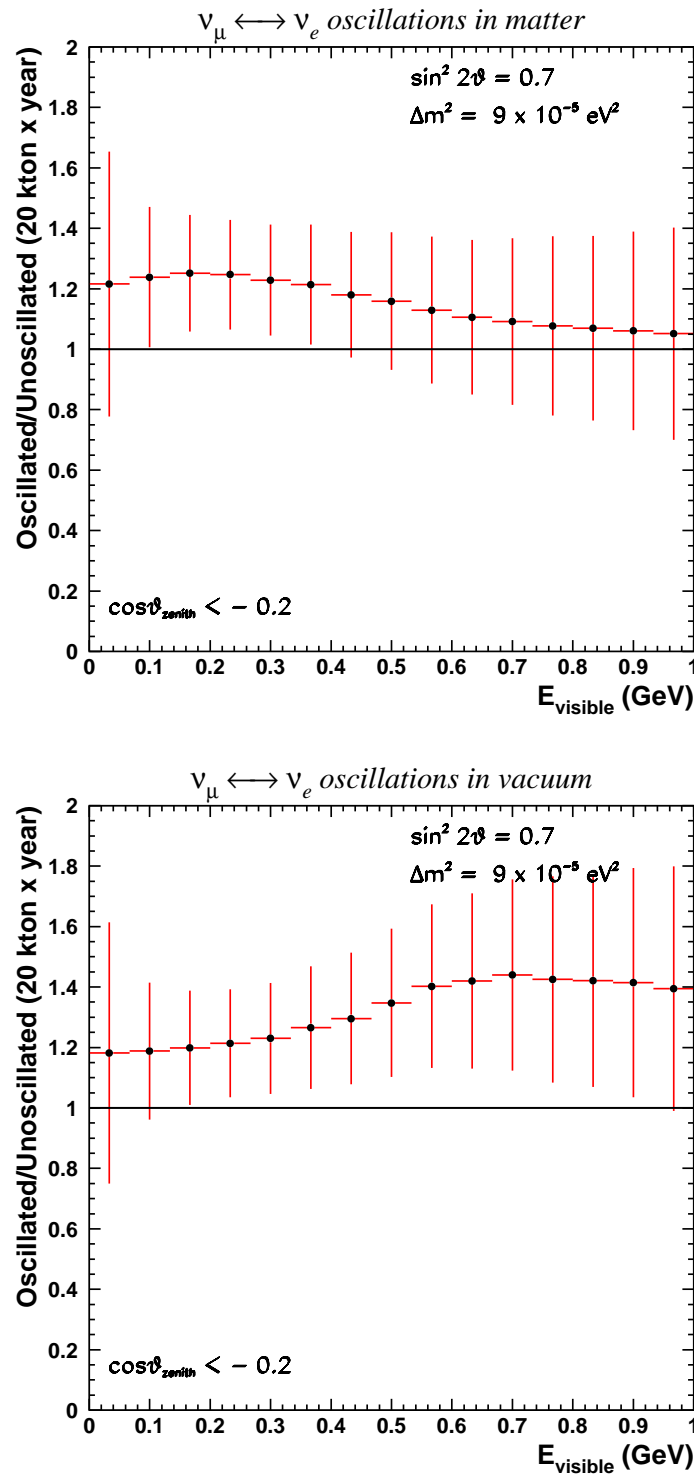
Figure 4.15: Ratio between oscillated and non oscillated events as a function of visible energy for both oscillation in matter (top plot) and in vacuum (bottom plot).

$\nu_\mu \leftrightarrow \nu_e$ oscillations in vacuum			
Exposure	ν_e CC	ν_e CC	ν_e CC excess
$(kton \times year)$	no oscillations	oscillations	(%)
5	125	153	23 ± 10
20	500	613	23 ± 5
50	1249	1533	23 ± 3
Cuts: $E_{vis} < 1$ GeV, $\cos\theta_{zenith} < -0.2$			
Oscillation parameters: $\Delta m^2 = 9 \times 10^{-5}$ eV^2, $\sin^2 2\theta = 0.7$.			

Table 4.5: Atmospheric neutrino electron events in the low energy region for $\nu_\mu \leftrightarrow \nu_e$ oscillations with $\Delta m^2 = 9 \times 10^{-5}$ eV^2, $\sin^2 2\theta = 0.7$.

Chapter 5

Test of a Calorimetric read-out in the $10\ m^3$ module

5.1 Introduction

The ICANOE detector design foresees the presence of a dedicated device for the calorimetric measurement of energy deposited in the LAr layers surrounding the imaging region.

This measurement is particularly important for the two LAr layers (about 30cm of thickness) interleaved between the imaging LAr region and the adjacent solid calorimetric targets, along the ν beam axis. In fact, a continuous calorimetric connection is thus established between the two regions, possibly with a spatial information.

Ionization charges deposited in LAr from through-going particles/showers outside the imaging volume are "naturally" transported onto the cryostat walls, due to the residual electric field established by the potential of the field shaping system (cathode and race-tracks) with respect to the grounded walls of the detector cryostat. Therefore, the easiest way to collect and read-out these charges may be provided by the insertion of a set of electrodes placed as close as possible to the walls. The proposed solution is provided by the installation of a set of planes of multi-layers printed boards (MLPB). From the charge collection one can obtain energy measurement by off-line cross calibration, including compensation factor for the hadronic component, obtained by a combined information from the imaging LAr region and the solid calorimeter.

To increase the drift-velocity of the charge deposited in these regions, the calorimetric electrodes may be positively biased (order of $+500V$). Dedicated electronic chains, from pre-amplifier to ADC, should also be foreseen and suitably matched to the signal amplitude and timing.

5.2 A test scheme for the $10m^3$ module

The ICARUS $10m^3$ module is presently being upgraded from its initial role of cryogenics and mechanics test facility into a fully equipped ICARUS detector prototype. Namely the wire chamber has been entirely instrumented, for the signal read-out connection of all the 1856 wires to the electronics boards, and a field shaping system, with $3.5{\times}2m^2$

cathode and six race-track squared rings, has been built and mounted in front of the wire planes, providing about 40 cm of maximum drift. The present configuration reproduces closely the T600 ICARUS configuration (except for the different drift length).

During the technical operations on the internal detector, a simple scheme to read-out the charge deposited in (one) non imaging LAr zone has been defined and implemented.

The adopted scheme makes use of a thin vetronite ($1mm \times 970mm \times 1286mm$) plane with Cu metallization on one side. The copper layer has been manufactured to obtain 16 long ($1286mm$) pads with $60mm$ width and $5mm$ gap in between (the first and last pads have reduced ($27.5mm$) width). Two such planes of pads have been vertically anchored by vetronite rods to the wire chamber mechanical structure, as shown in Fig.1 and Fig.2, covering almost entirely one of the two vertical sides of the race-track rings system.

The length of the sustaining rods is such that the pad planes (Cu side) are positioned at $30cm$ distance from the vertical side of the race-track rings. The distance to the cryostat wall was set at the minimum for a safe insertion of the chamber into the cryostat, i.e. about $1.5cm$. This distance establishes the capacitance of the pad: $\sim 250pF$ after LAr filling.

Two dedicated sets of connectors + flat cable (16 channels each), of the same type as for the wires, have been mounted and electrically connected to the corresponding planes, see details on Fig.1. The connection to the outer electronics is made possible using two spare feed-through connectors in one of the signal flanges.

The total capacitance of the single pad + cable set has been measured in air, after insertion into the cryostat. It amounts to about 450pF (400pF) for the lower (upper) plane of pads where 6m (5m) of flat cable (50pF/m) was used.

These values are within the range of capacitance of the wires of the imaging region and therefore the read-out signals from the pads can be read-out via the standard electronic chain in use for the wires. Only minor modification on the RC feedback circuit of the amplifier is required to allow longer electron drift time in the LAr calorimetric region.

A study of the electric field configuration, for a standard HV setting (cathode at -17.5kV and pads at +400V), has been performed and equipotential lines maps have been produced. In Fig.3 the top view of the map of equi-potential lines is shown with a schematic layout of the $10m^3$ internal detector (cathode, race-track rings, wire planes and frame supports) and of the cryostat walls. The planes of pads is shown close to the right side of the cryostat. Ionization tracks crossing the LAr calorimetric region have also been simulated to check the electron drift path onto the pads. An example is shown in Fig.4

A full test of this calorimetric technique will be performed during the operation of the $10m^3$ module.

Figure 5.1: The planes of pads mounted onto the $10m^3$ wire chamber frame. Connections and the signal flat cable are also visible. The distance between the plane and the mechanical frame is about 30 cm

Figure 5.2: The inner detector during the insertion into the 10m^3 cryostat. The two planes of calorimetric pads are visible at the left-hand side of the wire chamber mechanical structure.
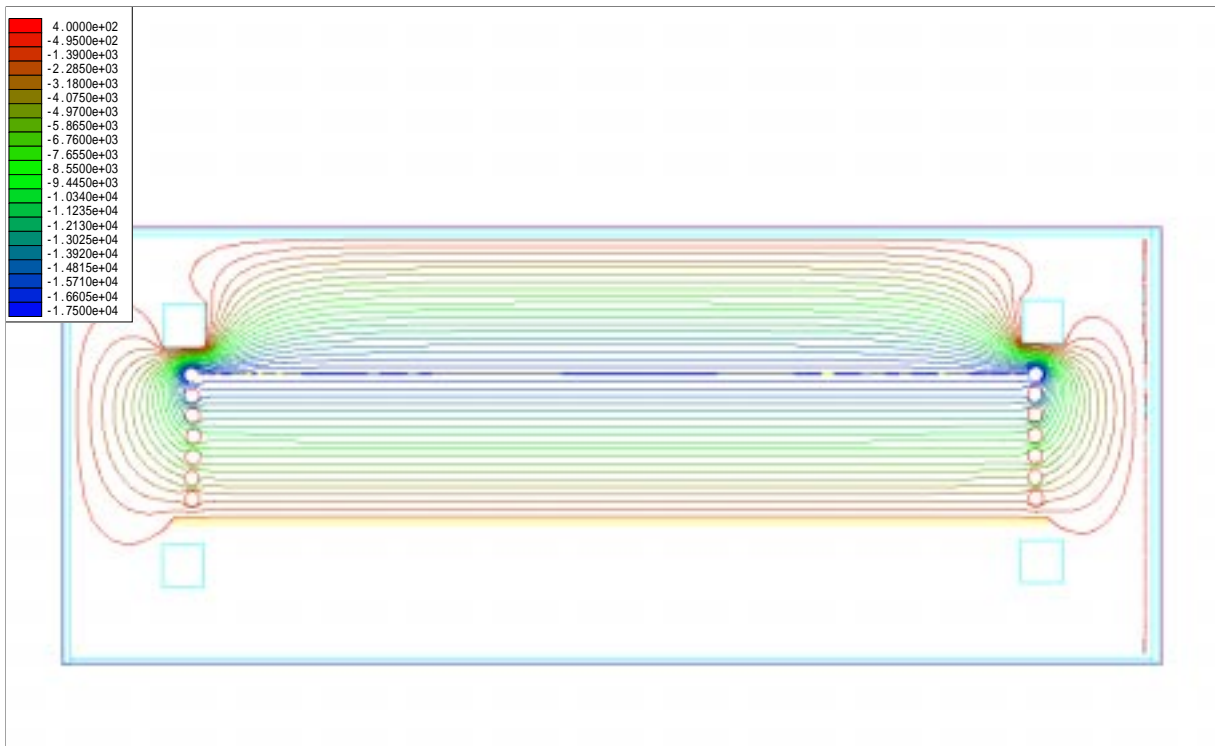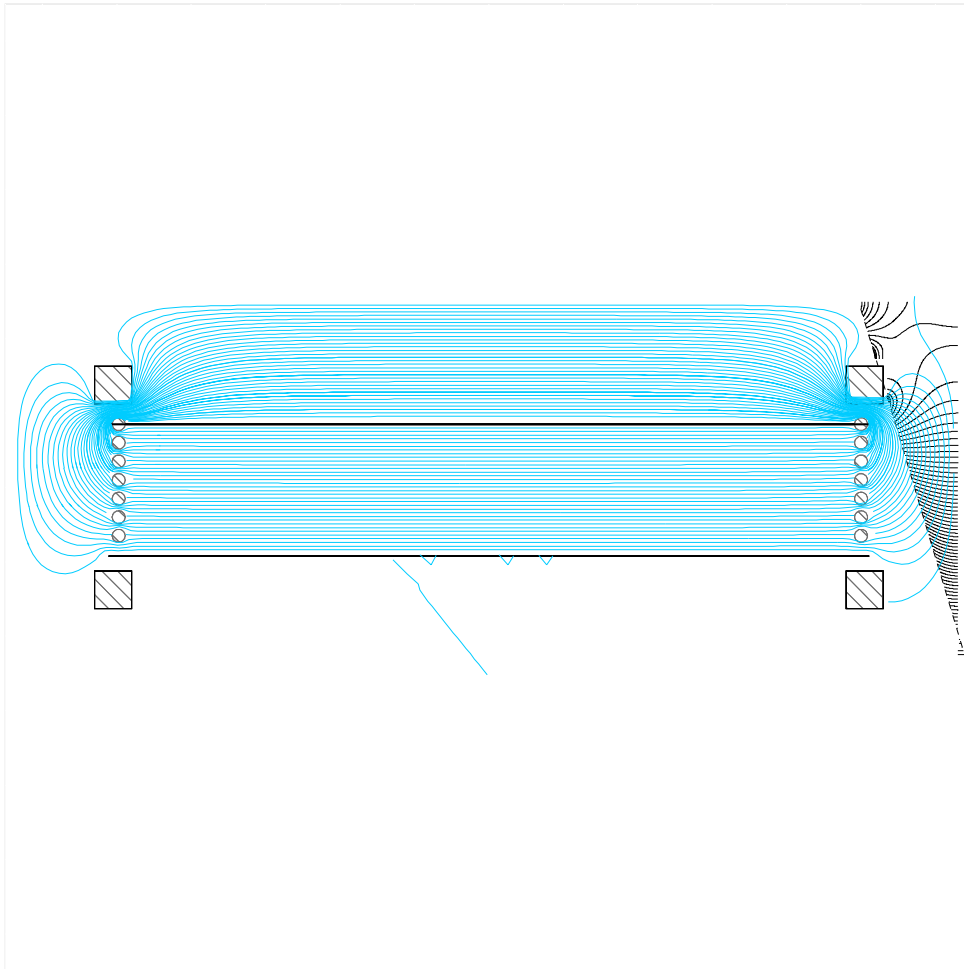
Figure 5.3: Top view of the equipotential lines map: pads are positioned close to the left-hand side wall

Figure 5.4: Ionization track crossing the LAr calorimetric region: map of the electron drift path

Bibliography

[1] ICARUS and NOE Collaborations *"ICANOE - Imaging and CAlorimetric Neutrino Oscillation Experiment"*, INFN/AE-99-17, LNGS-P21/99, CERN/SPSC 99-25, SPSC/P314

[2] R. Bailey et al., CERN-SL/99-o34(DI) and INFN/AE-99-05

[3] A. Ferrari and C. Rubbia, *"Muon momentum determination by multiple scattering in liquid argon"*, ICARUS/Internal Note 99/10, 1999

[4] G. Battistoni, A. Ferrari, P. Lipari, T. Montaruli, P.R. Sala and T. Rancati *"A 3-dimensional Calculation of Atmospheric Neutrino Flux"*, hep-ph/9907408, submitted to Astroparticle Physics

[5] G. Ambrosini et al., *Phys. Lett. B420 (1998) 225.*; G. Ambrosini et al., *Phys. Lett. B425 (1988) 208.*

[6] G. Collazuol, A. Ferrari, A. Guglielmi, P.R.Sala, "Neutrino beams: production models and experimental data", CERN OPEN-98-032 (1998), an enlarged version has been submitted to NIM A

[7] L. Camilleri, NOMAD presentation, SPSC open meeting, september 14th 1999)